

1 **Development of East Asia Regional**
2 **Reanalysis based on advanced hybrid gain**
3 **data assimilation method and evaluation**
4 **with E3DVAR, ERA-5, and ERA-Interim**
5 **reanalysis**

6
7
8 Eun-Gyeong Yang, Hyun Mee Kim^{*}, and Dae-Hui Kim

9 *Atmospheric Predictability and Data Assimilation Laboratory*

10 *Department of Atmospheric Science, Yonsei University, Seoul, Republic of Korea*

11
12
13
14 Submitted to *Earth System Science Data*

15 June 28, 2021

16 [Revision submitted on January 7, 2022](#)

17
18

^{*} *Corresponding author address:* Hyun Mee Kim, Department of Atmospheric Sciences,
Yonsei University, 50 Yonsei-ro, Seodaemun-gu, Seoul, 03722, Republic of Korea.

E-mail: khm@yonsei.ac.kr

19 **ABSTRACT**

20 The East Asia Regional Reanalysis (EARR) system is developed based on the advanced
21 hybrid gain data assimilation method (AdvHG) using Weather Research and Forecasting (WRF)
22 model and conventional observations. Based on EARR, the high-resolution regional reanalysis
23 and reforecast fields are produced with 12 km horizontal resolution over East Asia for 2010–
24 2019. The newly proposed AdvHG is based on the hybrid gain approach, weighting two
25 different analysis for an optimal analysis. The AdvHG is different from the hybrid gain in that
26 1) E3DVAR is used instead of EnKF, 2) 6 h forecast of ERA5 is used to be more consistent
27 with WRF, and 3) the pre-existing, state-of-the-art reanalysis is used. Thus, the AdvHG can be
28 regarded as an efficient approach to generate regional reanalysis dataset due to cost savings as
29 well as the use of the state-of-the-art reanalysis. The upper air variables of EARR are verified
30 with those of ERA5 for January and July 2017 and ~~the two-year period of 2017-2018~~—the ten-
31 year period of 2010-2019. For upper air variables, ERA5 outperforms EARR over two years,
32 whereas EARR outperforms (shows comparable performance to) ERA-I and E3DVAR for
33 January in 2017 (July in 2017). EARR better represents precipitation than ERA5 for January
34 and July in 2017. Therefore, though the uncertainties of upper air variables of EARR need to
35 be considered when analyzing them, the precipitation of EARR is more accurate than that of
36 ERA5 for both two seasons. The EARR data presented here can be downloaded from
37 <https://doi.org/10.7910/DVN/7P8MZT> for data on pressure levels and
38 <https://doi.org/10.7910/DVN/Q07VRC> for precipitation.

40 **1. Introduction**

41 Reanalysis datasets have been widely used in the socio-economical field as well as
42 meteorological and climate research areas all over the world. Most of reanalysis datasets
43 consist of global reanalysis whose spatial and temporal resolutions are relatively coarse (e.g.,
44 Schubert et al. 1993; Kalnay et al. 1996; Gibson et al. 1997; Kistler et al. 2001; Kanamitsu et
45 al. 2002; Uppala et al. 2005; Onogi et al. 2007; Bosilovich 2008; Saha et al. 2010; Dee et al.
46 2011; Rienecker et al. 2011; Bosilovich 2015; Kobayashi et al. 2015; Hersbach et al. 2020). As
47 the importance of regional reanalysis dataset emerged, many operational centers and research
48 institutes around the world have been producing the dataset in their own areas (Mesinger et al.
49 2006; Renshaw et al. 2013; Borsche et al. 2015; Bromwich et al. 2016; Jerney and Renshaw
50 2016; Zhang et al. 2017; Bromwich et al. 2018; Fukui et al. 2018; He et al. 2019; Ashrit et al.
51 2020).

52 The long-term high-resolution datasets are essential to investigate the past extreme
53 weather events which might be associated with mesoscale features such as heavy rainfall events
54 with high spatial and temporal variability which coarser-resolution model cannot represent.
55 The dynamical downscaling approaches can be a solution for generating high-resolution dataset,
56 but they have some issues with insufficient spin-up (Kayaba et al. 2016). Moreover, Fukui et
57 al. (2018) demonstrated that regional reanalysis over Japan assimilating only the conventional
58 observations had the potential to reproduce precipitation fields better than the dynamical
59 downscaling approaches. Ashrit et al. (2020) also found that the high-resolution regional
60 reanalysis over India showed substantial improvements of regional hydroclimatic features
61 during summer monsoon for the period of 1979-1993 compared to the global reanalysis ERA-
62 Interim (ERA-I, Dee et al. 2011) from ECMWF. Furthermore, He et al. (2019) revealed that
63 the pilot regional reanalysis over the Tibetan Plateau was able to represent more accurate

64 precipitation features as well as atmospheric humidity than the global reanalyses of ECMWF
65 (i.e., ECMWF's fifth-generation reanalysis (ERA5, Hersbach et al. 2020) and ERA-I).

66 As part of this effort, regional reanalysis over East Asia were produced based on the
67 Unified Model for the two-year period of 2013-2014 and it was confirmed that regional
68 reanalysis over East Asia is beneficial (Yang and Kim 2017; Yang and Kim 2019). However,
69 because UM was no longer available for generating regional reanalysis over East Asia, another
70 numerical weather prediction (NWP) model and its data assimilation (DA) method are required.

71 To find the most appropriate and cost-efficient DA method for a regional reanalysis over
72 East Asia, several DA methods were compared. Yang and Kim (2021) demonstrated that the
73 hybrid ensemble-variational data assimilation method (E3DVAR) shows the better
74 performance compared to three-dimensional variational data assimilation (3DVAR) and
75 ensemble Kalman filter (EnKF) over East Asia for January and July in 2016. However, it is
76 essential to confirm if this hybrid method is accurate enough to be used for a regional reanalysis
77 over East Asia. Thus, E3DVAR was compared with the latest and the previous reanalysis data
78 ~~from ECMWF (i.e., ECMWF's fifth-generation reanalysis (ERA5, Hersbach et al. 2020) and~~
79 ~~ERA-Interim (ERA-I, Dee et al. 2011))~~—from ECMWF (ERA5 and ERA-I) for (re)analysis
80 and (re)forecast variables and it was found that a performance for a regional reanalysis needs
81 to be further improved.

82 For this reason, a new advanced hybrid gain (AdvHG) data assimilation method, which
83 combines E3DVAR and ERA5 based on WRF model, is newly proposed and investigated in
84 this study. A hybrid gain data assimilation method has been developed as a new kind of hybrid
85 methods (Penny 2014). Based on this method, an advanced data assimilation method is newly
86 developed in this study. Finally, using this newly proposed DA method (AdvHG), East Asia
87 regional reanalysis (EARR) system is developed based on WRF model. ~~EARR datasets have~~
88 ~~been produced for ten-year period of 2010-2019 and are verified for two-year period of 2017-~~

89 ~~2018.~~ EARR datasets have been produced for ten-year period of 2010-2019 and are publicly
90 available (<https://dataverse.harvard.edu/dataverse/EARR>).

91 To investigate the accuracy and uncertainty of the state-of-the-art AdvHG DA algorithm
92 developed in this study, analysis and forecast atmospheric variables of E3DVAR, AdvHG,
93 WRF-based ERA-I, and WRF-based ERA5 are evaluated for January and July in 2017,
94 respectively. In addition, reforecast precipitation fields of ERA-I and ERA5 from ECMWF are
95 also verified and compared. In this study, the datasets are evaluated for two-month period
96 (January and July in 2017) or ten-year period (2010-2019) depending on the availability of
97 datasets. The reanalysis and (re)forecast fields of the EARR based on AdvHG and ERA5 are
98 verified for ten-year period (2010-2019). In section 2, the EARR system including model, data
99 assimilation method, and observations are explained. In section 3, the evaluation methods are
100 presented. The verification results of (re)analysis and (re)forecast variables are presented in
101 section 4. Section 4.1 presents evaluation results for wind, temperature, and humidity variables,
102 and section 4.2 presents those for precipitation (re)forecast. Section 5 presents data availability.
103 Lastly, summary and conclusions are presented in section 6.

104 **2. Reanalysis system**

105 *2.1. Model*

106 In this study, the Advanced Research Weather Research and Forecasting (WRF, v3.7.1)
107 model is used with 12-km horizontal resolution (540 x 432 grid points) and 50 vertical levels
108 (up to 5 hPa) ~~as shown in Fig. 1.~~ for East Asia domain shown in Fig. 1. The model settings and
109 physics scheme are summarized in Table 1. Analysis fields are obtained every 6 h (00, 06, 12,
110 and 18 UTC) via assimilation of conventional observations with a 6 h assimilation window,
111 and forecast fields are integrated up to 36 h. The ERA5 reanalysis (Hersbach et al. 2020) is
112 used as the first initial condition before the cycling, and as boundary conditions every 6 h.

113 2.2. Data assimilation methods

114 2.2.1. E3DVAR

115 The E3DVAR method is one of hybrid data assimilation methods, which use a static
116 climatological background error covariance (BEC) and ensemble-based flow-dependent BEC,
117 and couples the EnKF and 3DVAR (Zhang et al. 2013). E3DVAR is based on a cost function
118 of 3DVAR. In E3DVAR, EnKF provides flow-dependent BEC as well as updates perturbations
119 for ensemble members. Following Zhang et al. (2013),

$$J^b = J_s^b + J_e^b = \frac{1}{2} \delta \mathbf{x}^T \left[(1 - \beta) \mathbf{B} + \beta \mathbf{P}^f \circ \mathbf{C} \right]^{-1} \delta \mathbf{x} , \quad (1)$$

120 where J_s^b is a traditional cost function based on a static climatological BEC \mathbf{B} and J_e^b is an
121 additional cost function based on ensemble-based BEC \mathbf{P}^f . \mathbf{C} is a correlation matrix for
122 localization of the ensemble covariance \mathbf{P}^f . The weighting coefficient β between static and
123 ensemble-based BEC is set to 0.8 in this study. To account for model error for E3DVAR, multi-
124 physics scheme is applied to 40-member ensembles. Yang and Kim (2021) found that E3DVAR
125 is the most appropriate DA method among 3DVAR, EnKF, and E3DVAR methods over East
126 Asia. More detailed information on E3DVAR implemented in this study can be found in Yang
127 and Kim (2021).

128 2.2.2. ~~Advanced hybrid gain data assimilation method~~ Hybrid gain data assimilation method

129 In the last decade, the traditional hybrid methods have been widely used for many
130 operational centers and research institutes. Recently, Penny (2014) has proposed a new class
131 of hybrid gain methods combining desirable aspects of both variational and EnKF families of
132 algorithms by weighting analyses from 3DVAR and LETKF for an optimal analysis in the
133 Lorenz 40-component model. Since then, this algorithm has been implemented at ECMWF
134 (Bonavita et al. 2015) and at a hybrid global ocean DA system in National Centers for
135 Environmental Prediction (NCEP) (Penny et al. 2015).

136 The hybrid gain algorithm can be described with the following equations:

$$\mathbf{x}_{Hyb}^a = \alpha \mathbf{x}_{det}^a + (1 - \alpha) \overline{\mathbf{x}}^a, \quad (2)$$

137 where \mathbf{x}_{Hyb}^a , \mathbf{x}_{det}^a , and $\overline{\mathbf{x}}^a$ denote the hybrid analysis, deterministic analysis, and the ensemble
 138 mean analysis from the ensemble-based assimilation method, and α is a tunable parameter
 139 (Penny 2014, Houtekamer and Zhang 2016).

140 The hybrid gain method is different from traditional hybrid methods, in that a hybrid gain
 141 approach linearly combines analysis fields from EnKF and variational DA method to produce
 142 a hybrid gain analysis rather than linearly combining respective BECs (Penny 2014). Basically,
 143 the hybrid gain method is to hybridize two different Kalman gain matrices of ensemble-based
 144 [Eq. (4)] and variational data assimilation system [Eq. (5)] as in Eq. (3).

$$\hat{\mathbf{K}} = \beta_1 \mathbf{K}^f + \beta_2 \mathbf{K}^B + \beta_3 \mathbf{K}^B \mathbf{H} \mathbf{K}^f, \quad (3)$$

145 where

$$\mathbf{K}^f = \mathbf{P}^f \mathbf{H}^T (\mathbf{H} \mathbf{P}^f \mathbf{H}^T + \mathbf{R})^{-1}, \quad (4)$$

$$\mathbf{K}^B = \mathbf{B} \mathbf{H}^T (\mathbf{H} \mathbf{B} \mathbf{H}^T + \mathbf{R})^{-1}. \quad (5)$$

146 \mathbf{H} is an observation operator mapping the model state vector to observation space and \mathbf{R} is the
 147 observation error covariance matrix. The matrices \mathbf{P}^f and \mathbf{B} indicate the ensemble-based and
 148 the static climatological BEC, respectively. By choosing the specific coefficients ($\beta_1=1$, $\beta_2 =$
 149 α , $\beta_3 = -\alpha$), it can be written as in Eq. (6) and it can give an algebraically equivalent result
 150 with Eq. (2) (Penny 2014).

$$\hat{\mathbf{K}} = \mathbf{K}^f + \alpha \mathbf{K}^B (\mathbf{I} - \mathbf{H} \mathbf{K}^f). \quad (6)$$

151 One of advantages of the hybrid gain algorithm with respect to its development is that pre-
 152 existing operational systems can be used without significant modification for a hybrid analysis

153 (Penny 2014) and independent parallel development of respective methods is allowed
 154 (Houtekamer and Zhang 2016). Furthermore, the hybrid gain approach can be considered as a
 155 practical and straightforward method in the foreseeable future to combine advantageous
 156 features of both ensemble- and variational-based DA algorithms (Houtekamer and Zhang 2016).
 157 More detailed information on this algorithm can be found in Penny (2014).

158 2.2.3. Advanced hybrid gain data assimilation method

159 In this study, based on the hybrid gain approach, an advanced hybrid gain data assimilation
 160 method (AdvHG) is newly proposed as follows:

$$X_{AdvHG}^a = \alpha X_{ERA5}^{f(6h)} + (1 - \alpha) \bar{X}_{E3DVAR}^a, \quad (7)$$

161 where $X_{ERA5}^{f(6h)}$ denotes the 6 h forecast of ERA5 reanalysis based on WRF model and \bar{X}_{E3DVAR}^a
 162 denotes the analysis of E3DVAR (Fig. 2). In Eq. (7), α is a tunable parameter and is assigned
 163 to be 0.5 in this study. This advanced hybrid gain approach is different from the hybrid gain
 164 approach in that 1) E3DVAR analysis is used instead of EnKF, 2) 6 h forecast of ERA5 is used
 165 instead of deterministic analysis from variational DA method, and 3) the pre-existing and state-
 166 of-the-art reanalysis data (i.e., ERA5) is simply used instead of producing deterministic
 167 analysis by assimilation. The reasons for these different approaches proposed in this study are
 168 as follows:

169 1) E3DVAR is used instead of EnKF because Yang and Kim (2021) confirmed that
 170 E3DVAR outperforms EnKF for winter and summer seasons over East Asia.

171 2) Instead of deterministic analysis, the 6 h forecast of ERA5 based on WRF model is
 172 used to make the hybrid analysis more balanced and consistent with WRF model, because
 173 ERA5 reanalysis fields are based on its own modeling system with coarser resolution, which
 174 is different from that of this study.

175 3) European Centre for Medium-Range Weather Forecasts (ECMWF) reanalysis (ERA5)

176 is used instead of producing our own analysis fields from a variational DA method. This is a
177 very efficient approach because of the cost savings as well as the use of the high-quality latest
178 reanalysis from ECMWF assimilating all currently available observations with the state-of-the-
179 art and advanced technology.

180 Therefore, the approach proposed in this study is called as “advanced hybrid gain method”
181 (denoted as “AdvHG”).

182 2.3. Observations

183 The NCEP PrepBUFR [Prepared or QC'd data in BUFR (Binary Universal Form for the
184 Representation of meteorological data) format] conventional observations (global upper air and
185 surface weather observations, NCEP/NWS/NOAA/U.S.DOC 2008) are used every 6 h (00, 06,
186 12, and 18 UTC) for an assimilation by E3DVAR and AdvHG methods (Fig. 1). The PrepBUFR
187 is the output of the final process for preparing the observations to be assimilated in the different
188 NCEP analyses. For observations, rudimentary multi-platform quality control (QC) and more
189 complex platform-specific QC were conducted (e.g., surface pressure, rawinsonde heights and
190 temperature, wind profiler, aircraft wind and temperature) in NCEP (Keyser 2013).
191 Furthermore, if the innovations (i.e., observation minus background) of some observations are
192 greater than 5 times the observational error, then that observation is rejected during assimilation
193 procedure in this study.

194 The assimilated observations are as follows: the surface observations (SYNOP, METAR,
195 Ship, and Buoy), radiosonde observation (SOUND), upper-wind report (PILOT), wind profiler,
196 aircraft, atmospheric motion vector (AMV) wind from a geostationary satellite (GEOAMV),
197 and Scatterometer oceanic surface winds (Scatwind), and precipitable water vapor from global
198 positioning system (GPSPW). The observation errors depending on each observation platform,
199 variable, and vertical levels are assigned based on the default observation error statistics
200 provided in WRFDA system (Table 2). All observations are spatially thinned by 20 km except

201 for AMV thinned by 200 km as done by Warrick (2015), Cotton et al. (2016), and Shin [et al.](#)
202 (2016).

203 To evaluate 6 h accumulated precipitation simulated by E3DVAR, AdvHG, ERA-I, and
204 ERA5 over East Asia, global surface weather observations (NCEP PrepBUFR,
205 NCEP/NWS/NOAA/U.S.DOC 2008) are used every 6 h (00, 06, 12, and 18 UTC). For an
206 evaluation of the monthly precipitation fields, the world monthly surface station climatology
207 (NCDC/NESDIS/NOAA/U.S.DOC et al. 1981) over 4700 different stations (2600 in more
208 recent years) is used.

209 *2.4. Global reanalysis datasets*

210 To compare EARR generated with other reanalysis datasets, ERA5 (Hersbach et al. 2020)
211 and ERA-I (Dee et al. 2011) reanalysis are chosen. The horizontal resolutions of ERA-I and
212 ERA5 are approximately 79 km ([TL255](#)) and 31 km ([TL639](#)), respectively. Because ERA5 is
213 based on the operational system in 2016, improvements in model physics, numerics, data
214 assimilation, and additional observations over the last decade are the advantages of ERA5
215 (Hersbach et al. 2018).

216 ~~Because reforecast as well as reanalysis fields are verified in this study, for forecast fields,~~
217 ~~two different forecast fields from ECMWF (i.e., forecast based on WRF model and reforecast~~
218 ~~based on ECMWF model) are used. The WRF forecast fields (i.e., WRF-based ERA5, WRF-~~
219 ~~based ERA-I) using ERA5 and ERA-I as initial conditions are integrated with 12 km resolution.~~
220 ~~Secondly, reforecast fields based on ECMWF model (i.e., ERA5_fromECMWF, ERA-~~
221 ~~I_fromECMWF), provided and downloaded from ECMWF, are used. In this study, (re)forecast~~
222 ~~as well as reanalysis fields need to be verified. Regarding reanalysis and (re)forecast fields of~~
223 ~~ECMWF, reanalysis fields (i.e., ERA5 and ERA-I) downloaded from ECMWF are evaluated~~
224 ~~(Figs. 3 and 6). There are two different (re)forecast fields (e.g., ERA5_fromECMWF, WRF-~~
225 ~~based ERA5) used in this study. WRF-based ERA5 and ERA-I are forecast fields based on~~

WRF model with 12 km horizontal resolution where ERA5 and ERA-I are used as initial conditions, respectively. In contrast, ERA5 from ECMWF and ERA-I from ECMWF are reforecast fields based on ECMWF model not WRF model, so the reforecast fields of ERA5 and ERA-I are provided and downloaded from ECMWF. These reforecast fields are only used for evaluation of precipitation (Figs. 8 and 9). The (re)analysis and (re)forecast fields and corresponding experiments are explained in Table 3.

3. Evaluation method

3.1. Equitable threat score and Frequency bias index

Based on the contingency table (Table 24), ETS is defined as

$$ETS = \frac{A - A_r}{A + B + C - A_r}, \text{ where } A_r = \frac{(A + B)(A + C)}{A + B + C + D}. \quad (8)$$

The ETS range is from -1/3 to 1 and the value 1 for ETS is a perfect score. ETS is a more balanced score than Probability of Detection (POD) and False Alarm Ratio (FAR), because it is sensitive to both false alarms and misses (Wilson 2010).

FBI is defined as

$$FBI = \text{Bias} = \frac{A + B}{A + C}. \quad (9)$$

The FBI indicates whether the model tends to over-forecast (too frequently, FBI > 1) or under-forecast (not frequent enough, FBI < 1) events with respect to frequency of occurrence.

3.2 Probability of detection and False alarm ratio

Based on the contingency table (Table 24), POD is defined as

$$POD = \frac{A}{A + C} = \frac{\text{Hits}}{\text{Hits} + \text{Misses}}. \quad (10)$$

The POD range is from 0 to 1. POD is required to be used with FAR, because POD can be artificially improved by systematically over-forecasting the events (Wilson 2010).

245 FAR is defined as

$$\text{FAR} = \frac{B}{A+B} = \frac{\text{False alarms}}{\text{Hits} + \text{False alarms}}. \quad (11)$$

246 The range of FAR is from 0 to 1 and its lower score implies a higher accuracy.

247 3.3 Brier skill score

248 Verification of the performance of high-resolution forecast with the traditional verification
249 metrics (e.g., ETS, FBI) can be misleading due to double penalty, particularly for highly
250 variable fields (e.g., precipitation). Therefore, as one of spatial verification approaches that do
251 not require forecast to match point observation spatially, neighborhood (fuzzy) verification
252 method, which assumes that slightly displaced forecast can be acceptable and a local
253 neighborhood can define the degree of allowable displacement (Ebert 2008; Kim et al. 2015;
254 On et al. 2018), is used in this section. According to Ebert (2008), depending on the matching
255 strategy, neighborhood verifications can be categorized into two frameworks: ‘single
256 observation-neighborhood forecast (SO-NF)’ where neighborhood forecasts surrounding
257 observations are considered, and ‘neighborhood observation-neighborhood forecast (NO-NF)’
258 strategies where not only neighborhood forecasts but also neighborhood observations
259 surrounding observations are considered. Due to the absence of high-resolution gridded
260 precipitation observation data in East Asia, various verification scores widely used as
261 ‘neighborhood observation-neighborhood forecast (NO-NF)’ strategy are not available in this
262 study. Thus, in this section, Brier skill score as one of ‘single observation-neighborhood
263 forecast (SO-NF)’ strategy is introduced.

264 The Brier score (BS) is similar to the mean-squared error (MSE) and is defined as (Wilks
265 2006):

$$\text{BS} = \frac{1}{N} \sum_{i=1}^N (p_i - o_i)^2. \quad (12)$$

266 where p_i denotes the probability forecast, and o_i denotes the binary observation which is either
 267 0 or 1, and N is the total number of observations during the given period. Generally, Brier skill
 268 score (or Brier score) is used to verify ensemble forecasts which are able to calculate
 269 probabilistic forecasts (Kay et al. 2013; Kim and Kim 2017). However, Brier skill score can
 270 also be used for deterministic forecasts using a pragmatic post-processing procedure (Theis et
 271 al., 2005; Mittermaier ~~et al.~~ 2014), which derives probabilistic forecasts from deterministic
 272 forecasts at every model grid point by considering neighborhood forecast as *pseudo ensemble*.

$$\text{BSS} = 1 - \frac{\text{BS}}{\text{BS}_{\text{ref}}}, \quad (13)$$

273 where BS_{ref} is Brier score of reference. Brier skill score is skill score with respect to Brier score
 274 as in Eq. (13). For reference, a climatology or other forecast can be used either. In this study,
 275 the WRF-based ERA-I is considered as a reference.

276 3.4 Pattern correlation coefficient

277 The pattern correlation coefficient (PCC) is defined as Eq. (14) (Shiferaw et al. 2018; Yoo
 278 and Cho 2018; Park and Kim 2020).

$$\text{PCC} = \frac{\sum_{i=1}^N (x_i - \bar{x})(o_i - \bar{o})}{\left[\sum_{i=1}^N (x_i - \bar{x})^2 \sum_{i=1}^N (o_i - \bar{o})^2 \right]^{1/2}}, \quad (14)$$

279 where x_i and o_i are (re)forecast and observed precipitation at i th observation location and the
 280 over-bar indicates the averaged variables over N observed stations in the verification area.

281 4. Results

282 4.1 Evaluation of wind, temperature, and humidity variables

283 4.1.1 RMSE for January and July 2017

284 The analysis and forecast RMSEs of E3DVAR, AdvHG, the WRF-based ERA-I, and

285 WRF-based ERA5 are calculated for zonal wind, meridional wind, temperature, and Qvapor
286 (water vapor mixing ratio in WRF) variables against sonde observations at 00 and 12 UTC in
287 verification domain (dashed box in Fig. 1) for January and July in 2017 and averaged over each
288 month (Figs. ~~2, 3, and 4~~—3, 4, and 5).

289 ~~For analysis RMSE (Fig. 2), ERA5 is smaller than ERA-I for all levels and variables. In~~
290 ~~particular, the analysis RMSE difference between ERA5 and ERA-I is distinctive for wind. The~~
291 ~~vertically averaged wind RMSE of ERA5 for January (2.22 m s⁻¹) and July (1.98 m s⁻¹) in~~
292 ~~2017 is smaller by approximately 0.23 and 0.3 m s⁻¹ than that of ERA-I for January (2.45 m s⁻¹~~
293 ~~and July (2.28 m s⁻¹) in 2017. The analysis RMSE of E3DVAR is smaller than that of~~
294 ~~AdvHG for all pressure levels and variables, except for temperature in July at 1000 hPa and~~
295 ~~Qvapor in January and July at 1000 hPa. In general, the analysis RMSE of AdvHG for all~~
296 ~~variables is comparable to or greater than that of ERA5.~~ For analysis RMSE (Fig. 23), E3DVAR
297 is smaller than AdvHG for all pressure levels and variables, except for temperature in July at
298 1000 hPa and Qvapor in January and July at 1000 hPa. In general, the analysis RMSE of
299 AdvHG for all variables is comparable to or greater than that of ERA5. The analysis RMSE of
300 ERA5 is smaller than that of ERA-I for all levels and variables; in particular, the analysis
301 RMSE difference between ERA5 and ERA-I is distinctive for wind.

302 Regarding wind variables of analysis (Figs. ~~2a, b, c, and d~~3a, b, c, and d), E3DVAR is the
303 most closely fitted to observations except for the wind in upper troposphere in January,
304 followed by ERA5, AdvHG, and ERA-I. For temperature RMSE (Figs. ~~2e and f~~3e and f),
305 ~~E3DVAR is smaller than AdvHG and ERA5 is smaller than ERA-I. However, in January (Fig.~~
306 ~~2e), ERA5 RMSE is the smallest for upper troposphere and RMSEs of ERA5 and E3DVAR~~
307 ~~are similar to each other for lower troposphere. In July (Fig. 2f), overall E3DVAR RMSE is the~~
308 ~~smallest except for 1000 hPa.~~ E3DVAR is smaller than AdvHG. For Qvapor, RMSE in July is
309 much larger than that in January due to a monsoonal flow carrying moist air to East Asia. In

310 general, Qvapor RMSE of E3DVAR is the smallest, followed by ERA5, AdvHG, and ERA-I.
311 Therefore, for all variables, generally E3DVAR analysis fields are the most closely fitted to
312 observations. Since the analysis RMSE implies how much analysis fields are fitted to
313 observations rather than the accuracy of analysis itself, not only analysis RMSE but also
314 forecast RMSE should be considered

315 ~~For 24 h forecast RMSEs (Fig. 3), ERA5 RMSE is the smallest for all levels and variables~~
316 ~~for January and July in 2017. In January (Figs. 3a, c, e, and g), overall, the 24 h forecast RMSE~~
317 ~~of ERA5 is the smallest and that of ERA-I is the largest for all variables, and RMSEs of AdvHG~~
318 ~~and E3DVAR are greater than those of ERA5 and smaller than those of ERA-I. Regarding~~
319 ~~AdvHG and E3DVAR, in general, AdvHG is smaller than E3DVAR for all levels and variables.~~
320 ~~Thus, in January, ERA5 is the most accurate, followed by AdvHG, E3DVAR, and ERA-I.~~
321 ~~Meanwhile, for July (Figs. 3b, d, f, and h), ERA5 shows the smallest RMSE, and AdvHG and~~
322 ~~E3DVAR show comparable RMSE to ERA-I. For 24 h forecast fields in January (Figs. 4a, c,~~
323 ~~e, and g), overall, RMSEs of AdvHG and E3DVAR are greater than those of ERA5 and smaller~~
324 ~~than those of ERA-I, and AdvHG RMSE is smaller than E3DVAR RMSE for all levels and~~
325 ~~variables. Meanwhile, for July (Figs. 4b, d, f, and h), AdvHG and E3DVAR show comparable~~
326 ~~RMSE to ERA-I.~~

327 Furthermore, general features of 36 h forecast RMSE (Fig. 45) are similar to the 24 h
328 forecast RMSE (Fig. 34). However, particularly in January, the 36 h forecast RMSE differences
329 between ERA5 and ERA-I are more distinctive compared to those of 24 h forecast. In January,
330 the vertically averaged 36 h forecast RMSE differences of ERA5 and ERA-I are 0.52 m s^{-1} for
331 wind, 0.16 K for temperature, and 0.08 g kg^{-1} for Qvapor, whereas those of 24 h forecast are
332 0.4 m s^{-1} for wind, 0.11 K for temperature, and 0.06 g kg^{-1} for Qvapor. In addition, the 36 h
333 forecast RMSE differences between ERA5 and AdvHG for January are on average 0.1 m s^{-1}
334 for wind, 0.05 K for temperature, and 0.02 g kg^{-1} for Qvapor, which are even smaller compared

335 to those of 24 h forecast, implying that AdvHG is a lot more accurate than ERA-I for January
336 in 2017. For July, 36 h forecast RMSE of ERA5 is the smallest and RMSEs of AdvHG and
337 E3DVAR are similar to those of ERA-I.

338 4.1.2 RMSE and spread for the period of ~~2017-18-2010-2019~~

339 In this section, EARR produced in this study is verified for a longer period with WRF-
340 based ERA5. RMSE and spread of reanalyses and reforecasts based on AdvHG method are
341 calculated and averaged over the period of ~~2017-2018-2010-2019~~. The reanalyses and
342 (re)forecast fields are evaluated by calculating RMSE valid at 00 and 12 UTC and spread at 00,
343 06, 12, and 18 UTC.

344 The averaged RMSEs of reanalysis for ERA5 and EARR (denoted as AdvHG in Fig. ~~56~~)
345 and spread of analysis and 6 h forecast fields of EARR (AdvHG) are shown in Fig. ~~56~~. With
346 respect to spread, the ensemble spreads of analysis fields are smaller than those of 6 h forecast
347 fields, on average, by ~~0.16~~0.15 m s⁻¹ for wind, 0.04 K for temperature, and 0.02 g kg⁻¹ for
348 Qvapor, which is the well-known characteristics of ensemble-based data assimilation methods.
349 To be specific, the wind spread (Figs. ~~56~~a and b) is similar to or greater than the wind RMSE
350 except for the upper troposphere above 200 hPa, implying ensemble spread for wind is well
351 represented below 200 hPa. ~~Even if the ensembles for temperature (Fig. 5e) are underdispersive~~
352 ~~compared to RMSE of temperature, overall Qvapor spread (Fig. 5d) is well represented except~~
353 ~~for 1000 hPa and above 200 hPa. On the contrary, the ensembles for temperature and Qvapor~~
354 ~~(Figs. 6c and d) are underdispersive compared to their RMSEs.~~

355 ~~Regarding reanalysis RMSE, overall ERA5 RMSE is smaller than AdvHG RMSE for all~~
356 ~~variables (Fig. 5). The vertically averaged RMSEs of ERA5 are smaller by 0.15 m s⁻¹ for wind,~~
357 ~~0.08 K for temperature, and 0.01 g kg⁻¹ for Qvapor than those of AdvHG. Regarding reanalysis~~
358 ~~RMSE, overall AdvHG RMSE is greater than ERA5 RMSE for all variables (Fig. 6). The~~
359 ~~vertically averaged RMSEs of AdvHG are greater by 0.16 m s⁻¹ for wind, 0.09 K for~~

360 temperature, and 0.01 g kg⁻¹ for Qvapor than those of ERA5. Nonetheless, the wind RMSEs of
361 AdvHG are similar to those of ERA5 for the middle of troposphere (400–850 hPa), and the
362 Qvapor RMSEs of AdvHG are similar to those of ERA5 except for 1000 hPa.

363 In addition, regarding 24 h forecast RMSE, ~~ERA5 shows smaller RMSE than AdvHG for~~
364 ~~all variables (Fig. 6).~~ AdvHG shows larger RMSE than ERA5 for all variables (Fig. 7).
365 The vertically-averaged RMSE differences of wind, temperature, and Qvapor variables
366 between AdvHG and ERA5 are approximately 0.2 m s⁻¹, 0.07 K, and 0.03 g kg⁻¹, respectively.
367 These differences are smaller, compared to the 24 h forecast RMSE difference between ERA-
368 I and ERA5 shown in Fig. 34 (i.e., wind, temperatureTemp, and Qvapor RMSE difference: 0.4
369 m s⁻¹, 0.11 K, and 0.06 g kg⁻¹ for January 2017, 0.25 m s⁻¹, 0.05 K, and 0.04 g kg⁻¹ for July
370 2017).

371 4.2 Evaluation of precipitation for January and July in 2017.

372 4.2.1 Evaluation metrics

373 4.2.1.1 Equitable threat score and Frequency bias index

374 In this section, for the point-based Equitable threat score (ETS) and Frequency bias index
375 (FBI) based on Table 24, the 6 h accumulated precipitation fields based on the 6 h forecast of
376 E3DVAR, AdvHG, WRF-based ERA-I, WRF-based ERA5, ERA-I_fromECMWF, and
377 ERA5_fromECMWF are evaluated every 6 h (00, 06, 12, and 18 UTC) for January and July in
378 2017 (Fig. 78). Here, all the WRF-based precipitation fields are based on 12-km horizontal
379 resolution, and ERA-I_fromECMWF and ERA5_fromECMWF have 79- and 31-km horizontal
380 resolutions, respectively. Generally, ETS decreases as a threshold increases for both two
381 months (Figs. 78a and c). For January in 2017 (Fig. 78a), AdvHG ETS is the greatest among
382 others. Compared to precipitation reforecasts from ECMWF (i.e., ERA-I_fromECMWF,
383 ERA5_fromECMWF), AdvHG shows the higher ETS, indicating that AdvHG is able to
384 simulate more accurate precipitation fields than ERA-I and ERA5 from ECMWF in January

385 2017. Surprisingly, ETS of ERA5_fromECMWF for January in 2017 is the lowest among all
386 the results compared and is even lower than that of ERA-I_fromECMWF.

387 Since the precipitation reforecasts from ECMWF have not only coarser resolutions but
388 also different forecast model (i.e., the forecasting system of ECMWF), the precipitation
389 forecasts of ERA5 and ERA-I are additionally produced by using the same forecast model with
390 the same resolution as AdvHG and E3DVAR in this study, as explained in section 2.4. For
391 January 2017 (Fig. 78a), ETS of ERA5 (i.e., WRF-based ERA5) is higher than that of
392 ERA5_fromECMWF for all thresholds, whereas ETS of ERA-I (i.e., WRF-based ERA-I) is
393 lower than that of ERA-I_fromECMWF except for ~~strong-high~~ thresholds (8 and 16 mm (6 h)⁻¹)
394 1). The ERA5 ETS is greater than the ERA-I ETS, but is smaller than the AdvHG ETS. The
395 AdvHG shows the greatest ETS among others with the same resolution and forecast model,
396 and E3DVAR, ERA5, and ERA-I follow.

397 Regarding FBI in winter (Fig. 78b), ~~for strong thresholds for 4, 8, and 16 mm (6 h)⁻¹~~
398 thresholds, all the results show the FBI smaller than 1, implying the underestimation of
399 frequency of precipitation ~~for strong thresholds for high-threshold events. While FBIs of~~
400 ~~ERA5_fromECMWF and ERA-I_fromECMWF are greater than 1 for weak thresholds, those~~
401 ~~WRF-based results are similar to 1 or smaller than 1.~~ In general, AdvHG shows the FBI closest
402 to 1 among all the results, which is consistent with the greatest ETS of AdvHG. The E3DVAR
403 FBI is similar to the AdvHG FBI, and ERA5 and ERA-I FBIs are similar to each other. ~~FBIs~~
404 ~~of ERA5 and ERA-I are smaller than those of AdvHG and E3DVAR.~~

405 Meanwhile, overall, the ETS values for January whose maximum is around 0.4 (Fig. 78a)
406 are much greater than those for July in 2017 whose maximum is around 0.2 (Fig. 78c), implying
407 that the precipitation forecast in summer is more difficult than that in winter. The ETS
408 difference between the results in July is smaller than those in January. Particularly, for the
409 thresholds 4 and 8 mm (6 h)⁻¹, ETSs in July are similar to each other (Fig. 78c). Except for

410 those two thresholds, the ETS of ERA-I_fromECMWF is the smallest. At the threshold 16 mm
411 (6 h)⁻¹, ERA5 ETS is the highest, followed by AdvHG, E3DVAR, ERA-I, ERA5_fromECMWF,
412 and ERA-I_fromECMWF. At the threshold 0.5 and 1 mm (6 h)⁻¹, the E3DVAR ETS is the
413 greatest, followed by ERA5, AdvHG, ERA5_fromECMWF, ERA-I, and ERA-I_fromECMWF.

414 With respect to FBI in July 2017, the WRF-based results show the FBIs greater than 1,
415 whereas reforecast from ECMWF show the FBIs greater than 1 for ~~weak-0.5, 1, and 4 mm (6~~
416 ~~h)⁻¹ thresholds and smaller than 1 for higher thresholds (8 and 16 mm (6 h)⁻¹) strong thresholds~~
417 (Fig. 78d). For July in 2017, in general, ERA5_fromECMWF FBI is the closest to 1, followed
418 by E3DVAR, AdvHG, ERA5, ERA-I, and ERA-I_fromECMWF FBI.

419 4.2.1.2 Probability of detection and False alarm ratio

420 The Probability of Detection (POD or Hit Rate) and False Alarm Ratio (FAR) are
421 calculated for precipitation simulated from E3DVAR, AdvHG, WRF-based ERA-I, WRF-
422 based ERA5, ERA-I_fromECMWF, and ERA5_fromECMWF for January and July in 2017
423 (Fig. 89). For January in 2017, AdvHG POD is the greatest among the WRF-based results,
424 followed by E3DVAR, ERA5, and ERA-I (Figs. 89a). ~~Overall, the results of reforecast from~~
425 ~~ECMWF (i.e., ERA-I_fromECMWF and ERA5_fromECMWF) have greater POD than the~~
426 ~~WRF-based POD for weak thresholds, whereas those have smaller POD than the WRF-based~~
427 ~~POD for strong thresholds. Regarding FAR, notably, ERA5_fromECMWF shows extremely~~
428 ~~great FAR and ERA5 shows the smallest FAR among all the results, which is a consistent result~~
429 ~~with the smallest ETS of ERA5_fromECMWF.~~ In addition to the lowest ETS of
430 ERA5_fromECMWF for January in 2017 as discussed in the section 4.2.1.1, FAR of
431 ERA5_fromECMWF is extremely high with low POD in winter. ~~Therefore, especially for~~
432 ~~January in 2017, the precipitation fields simulated from ERA5_fromECMWF over East Asia~~
433 ~~are much less accurate than any other results from this study. Therefore, especially for January~~
434 ~~in 2017, the precipitation fields simulated from EARR (AdvHG) over East Asia are a lot more~~

435 accurate than those from ERA5_fromECMWF.

436 ~~For July in 2017, generally, ERA5 shows the largest POD, followed by AdvHG, ERA-I,~~
437 ~~E3DVAR, ERA5_fromECMWF (Figs. 8e and d). For July in 2017, generally, AdvHG shows~~
438 ~~the largest POD, except for ERA5 (Fig. 9c). The ERA-I POD shows the largest POD for weak~~
439 ~~thresholds and the smallest POD for strong thresholds, compared to other results.~~ With respect
440 to FAR, FAR values in July is-are much greater than those in January, which is consistent with
441 the ETS difference between these two seasons. ~~Overall, for strong thresholds, ERA-I shows~~
442 ~~the highest FAR and ERA-I_fromECMWF shows the smallest FAR. For weak thresholds, the~~
443 ~~ERA-I_fromECMWF shows the highest FAR and E3DVAR shows the smallest FAR among~~
444 ~~all the results.~~

446 4.2.1.3 Brier skill score

447 The neighborhood sizes are chosen to be $3\Delta x$, $5\Delta x$, $9\Delta x$, and $11\Delta x$, which are 36, 60,
448 108, and 132 km, respectively, and the thresholds 0.5, 1, 4, 8, and 16 mm (6 h)⁻¹ are considered.
449 The probabilistic precipitation forecasts are calculated at every model grid point depending on
450 neighborhood sizes and thresholds. Regarding each observation, the nearest model grid point
451 to observations is considered as the center of neighborhood. For verification, 6 h accumulated
452 precipitation fields are extracted from the first 0–6 h forecast fields of WRF-based ERA-I,
453 WRF-based ERA5, E3DVAR, and AdvHG every 6 h (00, 06, 12, and 18 UTC). BSSs of
454 ERA5_fromECMWF and ERA-I_fromECMWF are not calculated, because they have different
455 resolution from WRF-based results.

456 Based on the neighborhood approach, Brier skill score (BSS) is calculated depending on
457 different neighborhood sizes for January and July in 2017, respectively (Fig. 910). Because the
458 reference of Brier score is chosen as the ERA-I, the positive BSS implies better accuracy than
459 ERA-I. In general, for both two months, AdvHG BSS is greater than ERA5 BSS. Although the

460 E3DVAR BSS is the greatest in July 2017, the AdvHG BSS is the greatest in January 2017.

461 For January in 2017, as a neighborhood size increases, AdvHG and E3DVAR BSSs tend
462 to increase except for ERA5. Overall, AdvHG BSS is the greatest among other BSSs for all
463 thresholds for all neighborhood sizes. The ERA5 BSS is greater than E3DVAR BSS except for
464 16 mm (6 h)⁻¹. The highest BSS of AdvHG and the lowest BSS of ERA-I are consistent with
465 ETS result. Unlike greater E3DVAR ETS than ERA5 ETS, ERA5 BSS is greater than E3DVAR
466 BSS in January 2017.

467 For July 2017, while the ETS difference between the WRF-based results is not distinct
468 (Fig. 78c), the BSS difference is rather noticeable. Generally, E3DVAR BSS is the greatest
469 among other BSSs for all thresholds except for 16 mm (6 h)⁻¹ for neighborhood sizes 9 and 11.
470 Although E3DVAR BSS is the largest, AdvHG outperforms ERA5 and ERA-I. The worst
471 performance of ERA-I precipitation is consistent with ETS result. At ~~weak-0.5, 1, and 4 mm (6~~
472 ~~h)⁻¹ thresholds, E3DVAR BSS is the greatest, which is similar to ETS. For strong-At 8 and 16~~
473 ~~mm (6 h)⁻¹ thresholds, ERA5 ETS is the highest, followed by AdvHG and E3DVAR, whereas~~
474 overall E3DVAR BSS is the highest, followed by AdvHG and ERA5.

475 4.2.2 Spatial distribution

476 4.2.2.1 6 h accumulated precipitation with the pattern correlation coefficient

477 In this section, the spatial distributions of 6 h accumulated precipitation from the WRF-
478 based forecast and reforecast from ECMWF are compared. In addition, pattern correlation
479 coefficients (PCC) are calculated and shown at the bottom right of Figs. ~~10 and 11~~ and 12.

480 The PCC is computed according to the usual Pearson correlation operating on the N
481 observed point pairs of 6 h accumulated precipitation fields simulated from (re)forecast and
482 observations at the specific time. For the calculation of PCC, 6 h accumulated precipitation
483 fields from (re)forecast fields are interpolated bilinearly to the N observed points.

484 ~~Firstly, on 29th and 30th of January in 2017 (Fig. 10), it is noticeable that the precipitation~~

485 ~~of ERA5_fromECMWF does not match observations well over East Asia compared to other~~
486 ~~simulated precipitation fields. As shown in Fig. 10g, ERA5_fromECMWF incorrectly~~
487 ~~simulates precipitation over South East China, whereas other results do not forecast~~
488 ~~precipitation over this area. In addition, ERA5_fromECMWF overestimates precipitation over~~
489 ~~inland area of China (Fig. 10zz), whereas other results simulate precipitation similar to~~
490 ~~observations regarding its position and intensity. ERA5_fromECMWF also shows noticeably~~
491 ~~smaller PCC (Figs. 10g, n, and zz). Although PCC does not represent the exact accuracy or~~
492 ~~predictability of precipitation, the overall feature of PCC is consistent with the results found so~~
493 ~~far. In particular, PCCs of ERA5_fromECMWF are much smaller than those of other~~
494 ~~precipitation fields. For January in 2017, the averaged PCC of AdvHG is the greatest (i.e., 0.61)~~
495 ~~and that of ERA5_fromECMWF is the smallest (i.e., 0.46) (not shown). Firstly, on 29th and~~
496 ~~30th of January in 2017 (Fig. 11), it is noticeable that the precipitation fields of AdvHG match~~
497 ~~observations well over East Asia, whereas, in particular, those of ERA5_fromECMWF do not.~~
498 ~~For example, ERA5_fromECMWF overestimates precipitation over inland area of China (Fig.~~
499 ~~11zz), while AdvHG simulates precipitation similar to observations regarding its position and~~
500 ~~intensity (Fig. 11x). ERA5_fromECMWF also shows noticeably smaller PCC (Figs. 11g, n,~~
501 ~~and zz). Although PCC does not represent the exact accuracy or predictability of precipitation,~~
502 ~~the overall feature of PCC is consistent with the results found so far. For January in 2017, the~~
503 ~~averaged PCC of AdvHG is the greatest (i.e., 0.61) and that of ERA5_fromECMWF is the~~
504 ~~smallest (i.e., 0.46) (not shown).~~

505 ~~Secondly, for 1st and 2nd of July in 2017 (Fig. 11), overall, the precipitation simulated from~~
506 ~~ERA5_fromECMWF is well represented, compared to January in 2017 shown in Fig. 10. The~~
507 ~~ERA-I_fromECMWF fails to simulate heavy rain for summer season due to its coarse~~
508 ~~resolution. Furthermore, during July in 2017, ERA5 and ERA-I simulate heavier precipitation~~
509 ~~than AdvHG (not shown), which is consistent with larger FBI of ERA5 and ERA-I at strong~~

510 ~~thresholds.~~ For 1st and 2nd of July in 2017 (Fig. 12), in general, AdvHG, E3DVAR, and ERA5
511 well simulate not only overall features of precipitation fields but also their intensity. During
512 July in 2017, ERA5 and ERA-I simulate heavier precipitation than AdvHG (not shown), which
513 is consistent with larger FBI of ERA5 and ERA-I at higher thresholds. For one-month period
514 of July in 2017, the averaged PCC of ERA5 is the greatest (i.e., 0.37) and that of AdvHG is
515 0.34, but the PCC difference between ERA5 and AdvHG is not distinctive. Moreover, the
516 overall range of averaged PCC of different datasets in summer (i.e., 0.29-0.35) is smaller than
517 that in winter (i.e., 0.46-0.61), which is consistent with the seasonal difference of ETS in this
518 study.

519 4.2.2.2 Monthly accumulated precipitation

520 In this section, the monthly accumulated precipitation fields of rain gauge based
521 observations, E3DVAR, AdvHG, ERA-I, ERA5, ERA-I_fromECMWF, and
522 ERA5_fromECMWF are compared to each other for two one-month periods in January and
523 July in 2017, respectively.

524 ~~Although all the results similarly represent overall features of precipitation in January (Fig.~~
525 ~~12), ERA5_fromECMWF (Fig. 12g) simulates the overestimated precipitation over South~~
526 ~~China, compared to other results and observations, which is consistent with the results in the~~
527 ~~previous section as well as its larger FBI at weak thresholds shown in Fig. 7b. It is noticeable~~
528 ~~that all results fail to represent the observed precipitation area over Tibetan Plateau (25°–40°N,~~
529 ~~95–105°E). The monthly accumulated precipitation fields simulated by E3DVAR and AdvHG~~
530 ~~(Figs. 12b and c) are similar to each other, and E3DVAR and AdvHG produce the best fit to~~
531 ~~observed fields. Especially, for the north-western part of Japan (e.g., Chugoku and Kinki),~~
532 ~~E3DVAR and AdvHG are able to represent precipitation correctly, whereas ERA-~~
533 ~~I_fromECMWF and ERA5_fromECMWF fail to do so (Fig. 12).~~ The monthly accumulated
534 precipitation fields simulated by E3DVAR and AdvHG (Figs. 13b and c) are similar to each

535 other, and E3DVAR and AdvHG produce the best fit to observed fields. Especially, for the
536 north-western part of Japan (e.g., Chugoku and Kinki), E3DVAR and AdvHG are able to
537 represent precipitation correctly, whereas ERA-I_fromECMWF and ERA5_fromECMWF fail
538 to do so (Fig. 13). Moreover, although all the results similarly represent overall features of
539 precipitation in January (Fig. 13), ERA5_fromECMWF (Fig. 13g) simulates the overestimated
540 precipitation over South China, which is consistent with the results in the previous section as
541 well as its larger FBI at lower thresholds (0.5 and 1 mm (6 h)⁻¹) shown in Fig. 8b. It is noticeable
542 that all results fail to represent the observed precipitation area over Tibetan Plateau (25°–40°N,
543 95°–105°E).

544 For the monthly accumulated precipitation in July 2017, overall, the ERA5_fromECMWF
545 (Fig. 143g) and the WRF-based results (Fig. 143b, c, and e) except for ERA-I (Fig. 134d) well
546 simulate precipitation similar to observations. ~~ERA-I_fromECMWF is not able to simulate~~
547 ~~heavy precipitation over Korea. For western and southern part of Japan, while ERA-~~
548 ~~I_fromECMWF and ERA5_fromECMWF simulate similar precipitation fields to observed~~
549 ~~fields, WRF-based results overestimate precipitation over these regions. Compared to ERA-~~
550 ~~I_fromECMWF and ERA5_fromECMWF, the WRF-based results tend to overestimate~~
551 ~~precipitation in South China, Korea, and Japan. This is consistent with the result in Fig. 7d, in~~
552 ~~which FBIs from WRF-based results are generally greater than 1 for strong thresholds, whereas~~
553 ~~those from ECMWF are smaller than 1. The WRF-based results including AdvHG overestimate~~
554 ~~precipitation over western and southern part of Japan, while ERA-I_fromECMWF and~~
555 ~~ERA5_fromECMWF simulate similar precipitation fields to observed fields. The WRF-based~~
556 ~~results tend to overestimate precipitation in South China, Korea, and Japan, compared to ERA-~~
557 ~~I_fromECMWF and ERA5_fromECMWF. This is consistent with the result in Fig. 8d, in which~~
558 ~~FBIs from WRF-based results are generally greater than for higher thresholds (8 and 16 mm (6~~
559 ~~h)⁻¹), whereas those from ECMWF are smaller than 1.~~

560 Even though detailed precipitation features of WRF-based results are different, overall
561 features of precipitation from WRF-based results are similar to each other, which implies that
562 predictability of precipitation strongly depends on the physics schemes as well as NWP model,
563 especially for summer season. According to Que et al. (2016), depending on the combinations
564 of physics options in WRF model, the spatial distribution of precipitation can be significantly
565 different over Asian summer monsoon area and YSU PBL scheme which is used in this study
566 tends to overestimate precipitation over the same area. Thus, different physics options could
567 simulate the different spatial distribution of precipitation.

568 In addition, compared to ERA5 based on WRF model (Fig. 134e), ECMWF model for
569 ERA5_fromECMWF (Fig. 134g) seems to suppress precipitation. Thus, WRF model with the
570 physics schemes used in this study might simulate more precipitation than ECMWF model,
571 although the initial condition is the same. Therefore, it is important to consider the consistency
572 of the systems for data assimilation and forecast model for a good performance of ~~precipitation.~~
573 forecast weather variables like precipitation.

574 **5. Data Availability**

575 The EARR data presented in this study are available every 6 h (i.e., 00, 06, 12, and 18
576 UTC) for the period of 2010-2019 from Harvard Dataverse Repository
577 (<https://dataverse.harvard.edu/dataverse/EARR>). The EARR 6 hourly data on pressure levels
578 (<https://doi.org/10.7910/DVN/7P8MZT>, Yang and Kim 2021b) and 6 hourly precipitation data
579 (<https://doi.org/10.7910/DVN/Q07VRC>, Yang and Kim 2021c) are provided in NetCDF file
580 format.

581 The EARR 6 hourly data on pressure levels (Yang and Kim 2021b) include u-component
582 of wind, v-component of wind, temperature, geopotential height, and specific humidity
583 variables of reanalysis on pressure levels (i.e., 925, 850, 700, 500, 300, 200, 100, and 50 hPa).

584 The EARR 6 hourly precipitation data (Yang and Kim 2021c) contain 6 h accumulated total
585 precipitation variable of 6 h reforecast on single level. The 6 h accumulated total precipitation
586 is obtained from 6 h reforecast field which is integrated for 6 h from reanalysis field every 6 h
587 (i.e., 00, 06, 12 and 18 UTC).

588 **6. Summary and conclusions**

589 In this study, to develop the regional reanalysis system over East Asia, the advanced
590 hybrid gain algorithm (AdvHG) is newly proposed and evaluated with traditional hybrid DA
591 method (E3DVAR) as well as existing reanalyses from ECMWF (ERA5 and ERA-I) for
592 January and July in 2017. ~~The East Asia Regional Reanalysis (EARR) system is developed
593 based on the AdvHG as the data assimilation method using WRF model and conventional
594 observations, and the high-resolution regional reanalysis and reforecast fields with 12 km
595 horizontal resolution are produced over East Asia for the ten-year period of 2010–2019. The
596 East Asia Regional Reanalysis (EARR) system is developed based on the AdvHG as the data
597 assimilation method using WRF model and conventional observations. The high-resolution
598 regional reanalysis and reforecast fields over East Asia with 12 km horizontal resolution are
599 produced and evaluated against observations with ERA5 for the ten-year period of 2010–2019.~~

600 The AdvHG newly proposed in this study is based on the hybrid gain approach, weighting
601 analyses from variational-based and ensemble-based DA algorithms to generate optimal
602 hybrid analysis, which can play an important role as a simple and practical method in the
603 foreseeable future to take advantage of each strength of two different DA methods. The
604 advanced hybrid gain method is different from the hybrid gain approach in that 1) E3DVAR is
605 used instead of EnKF, 2) 6 h forecast of ERA5 is used instead of deterministic analysis for a
606 more balanced and consistent analysis with WRF model, and 3) the pre-existing and state-of-
607 the-art reanalysis data (i.e. ERA5) is simply used instead of producing our own analysis fields

608 from a variational DA method. Thus, it can be regarded as an efficient approach to generate
609 regional reanalysis dataset because of cost savings as well as the use of the state-of-the-art
610 reanalysis from ECMWF that assimilates all available observations.

611 For a verification, the latest ECMWF reanalysis and reforecast datasets (i.e., ERA5 and
612 ERA-I) are used. With respect to forecast variables, two different forecast fields of ECMWF
613 are used: 1) reforecast fields from ECMWF (i.e., ERA5_fromECMWF and ERA-
614 I_fromECMWF) and 2) forecast fields (i.e., WRF-based ERA5 and WRF-based ERA-I)
615 integrated in WRF model with 12 km resolution using ERA5 and ERA-I as initial conditions.

616 ~~To evaluate this newly proposed algorithm, analysis and forecast wind, temperature, and~~
617 ~~humidity variables are evaluated with respect to RMSE and spread for January and July in 2017.~~

618 Analysis and forecast wind, temperature, and humidity variables of AdvHG are evaluated with
619 ERA5 for the ten-year period and evaluated with five different experiments (i.e., E3DVAR,
620 ERA5, ERA-I, ERA5_fromECMWF, ERA-I_fromECMWF) for January and July in 2017.

621 Overall, the analysis RMSE of E3DVAR is the smallest among others but comparable to that
622 of ERA5, especially for January in 2017. Regarding forecast variables, AdvHG outperforms
623 E3DVAR ~~and ERA5 outperforms ERA-I~~ for January and July in 2017. Although ERA5
624 outperforms AdvHG for upper air variables for two seasons in 2017, AdvHG outperforms
625 ERA-I in January and shows comparable performance to ERA-I in July. Additionally the
626 verification results of AdvHG and ERA5 for the period of 2010-20197-18 are consistent with
627 those for two one-month period in 2017.

628 The precipitation forecast variables are also verified regarding a neighborhood-based
629 verification score (i.e., Brier skill score) as well as the point-based verification scores (i.e., ETS,
630 FBI, POD, and FAR). According to the point-based verification scores, the precipitation
631 forecast of AdvHG in January is the most accurate, followed by E3DVAR, ERA5, ERA-I. ~~The~~
632 ~~precipitation reforecast of ERA5_fromECMWF shows the worst performance with the lowest~~

633 ~~ETS and the highest FAR among other results in January.~~ For July, overall ETS values of all
634 results are relatively lower compared to those in January, implying the lower predictability in
635 summer season. ~~For July, ERA5 shows the greatest ETS for strong thresholds followed by~~
636 ~~AdvHG and E3DVAR, and E3DVAR ETS is the greatest followed by ERA5 and AdvHG for~~
637 ~~weak thresholds. However, the ETS differences between the results are not distinctive.~~ In
638 addition, the ETS differences between the results are not distinctive in July. For higher
639 thresholds (8 and 16 mm (6 h)⁻¹) in July, AdvHG ETS is greater than E3DVAR ETS and smaller
640 than ERA5 ETS, whereas E3DVAR ETS is the greatest followed by ERA5 and AdvHG for
641 lower thresholds (0.5 and 1 mm (6 h)⁻¹).

642 To prevent from double penalty when verifying a highly variable data with high resolution
643 (e.g., precipitation), Brier skill score (BSS) based on neighborhood approach is calculated for
644 6 h accumulated precipitation forecasts depending on different neighborhood sizes for January
645 and July in 2017. In general, BSS of AdvHG is greater than that of ERA5 and ERA-I for both
646 two months. Although the E3DVAR BSS is the greatest in July 2017, the AdvHG BSS is the
647 greatest in January 2017.

648 Lastly, the spatial distributions of 6 h and monthly accumulated precipitation forecast for
649 AdvHG, E3DVAR, ERA-I, ERA5, ERA-I_fromECMWF, and ERA5_fromECMWF are
650 compared with rain-gauge based observations. For January 2017, it is noticeable that AdvHG
651 precipitation is the closest to observations with highest PCC (i.e., 0.61) and
652 ERA5_fromECMWF overestimates precipitation over South China with the lowest PCC (i.e.,
653 0.46). ~~For July in 2017, due to a coarse resolution of ERA-I_fromECMWF, it fails to represent~~
654 ~~heavy rain over East Asia. Meanwhile, the WRF-based results tend to overestimate~~
655 ~~precipitation compared to ERA-I_fromECMWF and ERA5_fromECMWF.~~ For July in 2017,
656 the WRF-based results tend to overestimate precipitation compared to ERA-I_fromECMWF
657 and ERA5_fromECMWF. In addition, even though the averaged PCC of ERA5 (i.e., 0.37) is

658 slightly greater than that of AdvHG (i.e., 0.34), the PCC difference between ERA5 and AdvHG
659 is not distinctive and overall range of averaged PCC of all datasets in summer (i.e., 0.29-0.357)
660 is smaller than that in winter (i.e., 0.46-0.6).

661 In conclusion, for upper air variables, overall, ERA5 outperforms EARR based on AdvHG,
662 but the RMSE difference between ERA5 and EARR (AdvHG) is smaller than that between
663 ERA5 and ERA-I. In addition, EARR outperforms ERA-I for January 2017 and shows
664 comparable performance to ERA-I for July 2017. On the contrary, according to the evaluation
665 results of precipitation, in general, EARR better represents precipitation than ERA5 as well as
666 ERA5_fromECMWF for January and July in 2017. Even if E3DVAR precipitation is better
667 represented than EARR precipitation for July, the difference is not considerable for July and
668 EARR better simulates precipitation for January than E3DVAR. Therefore, although the
669 uncertainties of upper air variables of EARR should be considered when analyzing them, the
670 precipitation reforecast of EARR is more accurate than that of ERA5 for both two seasons.

671

672 **Author contribution**

673 Hyun Mee Kim proposed the main scientific ideas and Eun-Gyeong Yang contributed the
674 supplementary ideas during the process. Eun-Gyeong Yang developed the reanalysis system
675 and produced the 10-year regional reanalysis data. Eun-Gyeong Yang and Hyun Mee Kim
676 analyzed the simulation results and completed the manuscript. Dae-Hui Kim contributed to
677 analyzing the reanalysis data and to the preparation of software and computing resources for
678 the reanalysis system.

679

680 **Competing interests**

681 The authors declare that they have no competing interests.

682

683 **Acknowledgments**

684 The authors appreciate reviewers for their valuable comments. This study was supported by a
685 National Research Foundation of Korea (NRF) grant funded by the South Korean government
686 (Ministry of Science and ICT) (Grant 2021R1A2C1012572) and the Yonsei Signature Research
687 Cluster Program of 2021 (2021-22-0003). This study was carried out by utilizing the
688 supercomputer system supported by the National Center for Meteorological Supercomputer of
689 Korea Meteorological Administration and Korea Research Environment Open NETWORK
690 (KREONET) provided by the Korea Institute of Science and Technology Information. The
691 authors gratefully acknowledge the late Dr. Fuqing Zhang for collaborations at the earlier
692 stages of this study.

693

694

695 **References**

- 696 Ashrit, R., S. Indira Rani, S. Kumar, S. Karunasagar, T. Arulalan, T. Francis, A. Routray, S. I. Laskar,
697 S. Mahmood, P. Jerney, A. Maycock, R. Renshaw, J. P. George, and E. N. Rajagopal, 2020:
698 IMDAA Regional Reanalysis: Performance Evaluation During Indian Summer Monsoon
699 Season. *Journal of Geophysical Research: Atmospheres*, **125**(2), e2019JD030973.
- 700 Bonavita, M., M. Hamrud, and L. Isaksen, 2015: EnKF and hybrid gain ensemble data assimilation.
701 Part II: EnKF and hybrid gain results. *Monthly Weather Review*, **143**(12), 4865-4882.
- 702 Borsche, M, A. K. Kaiser-Weiss, P. Undén, and F. Kaspar, 2015: Methodologies to characterize
703 uncertainties in regional reanalyses. *Adv. Sci. Res.*, **12**, 207-218.
- 704 Bosilovich, M., 2008: NASA's modern era retrospective-analysis for research and applications:
705 Integrating Earth observations. Earthzine, 26 September 2008. [Available online at
706 www.earthzine.org/2008/09/26/nasas-modern-era-retrospective-analysis/.]
- 707 Bosilovich, M., R. Lucchesi, and M. Suarez, 2015: MERRA-2: File specification. NASA GMAO Office
708 Note 9, 73 pp., <http://gmao.gsfc.nasa.gov/pubs/docs/Bosilovich785.pdf>.
- 709 Bromwich, D. H., A. B. Wilson, L. Bai, Z. Liu, M. Barlage, C. F. Shih, S. Maldonado, K. M. Hines, S.-
710 H. Wang, J. Woollen, B. Kuo, H.-C. Lin, T.-K. Wee, M. C. Serreze, and J. E. Walsh, 2018: The
711 Arctic system reanalysis, version 2. *Bulletin of the American Meteorological Society*, **99**(4),
712 805-828.
- 713 Bromwich, D. H., A. B. Wilson, L. S. Bai, G. W. Moore, and P. Bauer, 2016: A comparison of the
714 regional Arctic System Reanalysis and the global ERA-Interim Reanalysis for the Arctic.
715 *Quarterly Journal of the Royal Meteorological Society*, **142**(695), 644-658.
- 716 Cotton, J., M. Forsythe, F. Warrick, K. Salonen, N. Bormann, and K. Lean, 2016: AMVs in the Tropics:
717 use in NWP, data quality and impact, Joint ECMWF/ESA Workshop on 'Tropical modeling,
718 observations and data assimilation [Available online at <https://www.ecmwf.int/node/16865>]
- 719 Dee, D. P., S. M. Uppala, A. J. Simmons, P. Berrisford, P. Poli, S. Kobayashi, U. Andrae, M. A.
720 Balmaseda, G. Balsamo, P. Bauer, P. Bechtold, A. C. M. Beljaars, L. van de Berg, J. Bidlot, N.
721 Bormann, C. Delsol, R. Dragani, M. Fuentes, A. J. Geer, L. Haimberger, S. B. Healy, H.

722 Hersbach, E. V. Hólm, L. Isaksen, P. Kållberg, M. Köhler, M. Matricardi, A. P. McNally, B. M.
723 Monge-Sanz, J.-J. Morcrette, B.-K. Park, C. Peubey, P. de Rosnay, C. Tavalato, J.-N. Thépaut,
724 and F. Vitart, 2011: The ERA-Interim reanalysis: configuration and performance of the data
725 assimilation system. *Q. J. R. Meteorol. Soc.*, **137**, 553–597. doi: 10.1002/qj.828

726 Ebert, E. E., 2008: Fuzzy verification of high-resolution gridded forecasts: a review and proposed
727 framework. *Meteorological Applications: A journal of forecasting, practical applications,*
728 *training techniques and modelling*, **15**(1), 51-64.

729 Fukui, S., T. Iwasaki, K. Saito, H. Seko, and M. Kunii, 2018: A feasibility study on the high-resolution
730 regional reanalysis over Japan assimilating only conventional observations as an alternative to
731 the dynamical downscaling. *Journal of the Meteorological Society of Japan*. **96**(6), 565-585.

732 Gibson, J. K., P. Kållberg, S. Uppala, A. Nomura, A. Hernandez, E. Serrano, 1997: ERA Description.
733 *ECMWF Re-Analysis Final Report Series*, **1**, 71pp.

734 Grell, G. A., and S. R. Freitas, 2014: A scale and aerosol aware stochastic convective parameterization
735 for weather and air quality modeling. *Atmos. Chem. Phys*, **14**(10), 5233-5250.

736 [He, J., F. Zhang, X. Chen, X. Bao, D. Chen, H. M. Kim, H.-W. Lai, L. R. Leung, X. Ma, Z. Meng, T.](#)
737 [Ou, Z. Xiao, E.-G. Yang, and K. Yang, 2019: Development and evaluation of an ensemble-based](#)
738 [data assimilation system for regional reanalysis over the Tibetan Plateau and surrounding](#)
739 [regions, *Journal of Advances in Modeling Earth Systems*, **11**\(8\), 2503-2522.](#)

740 Hersbach, H., B. Bell, P. Berrisford, S. Hirahara, A. Horányi, J. Muñoz-Sabater, J. Nicolas, C. Peubey,
741 R. Radu, D. Schepers, A. Simmons, C. Soci, S. Abdalla, X. Abellan, G. Balsamo, P. Bechtold,
742 G. Biavati, J. Bidlot, M. Bonavita, G. D. Chiara, P. Dahlgren, D. Dee, M. Diamantakis, R.
743 Dragani, J. Flemming, R. Forbes, M. Fuentes, A. Geer, L. Haimberger, S. Healy, R. J. Hogan, E.
744 Hólm, M. Janisková, S. Keeley, P. Laloyaux, P. Lopez, C. Lupu, G. Radnoti, P. de Rosnay, I.
745 Rozum, F. Vamborg, S. Villaume, and J.-N. Thépaut, 2020: The ERA5 global reanalysis.
746 *Quarterly Journal of the Royal Meteorological Society*, **146**(730), 1999-2049.

747 Hersbach, H., P. de Rosnay, B. Bell, D. Schepers, A. Simmons, C. Soci, S. Abdalla, M. Alonso
748 Balmaseda, G. Balsamo, P. Bechtold, P. Berrisford, J. Bidlot, Eric. de Boissésou, M. Bonavita,

749 P. Browne, R. Buizza, P. Dahlgren, D. Dee, R. Dragani, M. Diamantakis, J. Flemming, R. Forbes,
750 A. Geer, T. Haiden, E. Hólm, L. Haimberger, R. Hogan, A. Horányi, M. Janisková, P. Laloyaux,
751 P. Lopez, J. Muñoz-Sabater, C. Peubey, R. Radu, D. Richardson, J.-N. Thépaut, F. Vitart, X.
752 Yang, E. Zsótér, and H. Zuo, 2018: Operational global reanalysis: progress, future directions
753 and synergies with NWP, *ECMWF ERA report series*, N27.

754 Hong, S.-Y., Y. Noh, and J. Dudhia, 2006: A new vertical diffusion package with an explicit treatment
755 of entrainment processes. *Monthly Weather Review*, **134**(9), 2318-2341.

756 Houtekamer, P. L., and F. Zhang, 2016: Review of the ensemble Kalman filter for atmospheric data
757 assimilation. *Monthly Weather Review*, **144**(12), 4489-4532.

758 Iacono, M. J., J. S. Delamere, E. J. Mlawer, M. W. Shephard, S. A. Clough, and W. D. Collins, 2008:
759 Radiative forcing by long-lived greenhouse gases: Calculations with the AER radiative transfer
760 models. *Journal of Geophysical Research: Atmospheres*, **113**(D13).

761 Jerney, P. M., and R. J. Renshaw, 2016: Precipitation representation over a two-year period in regional
762 reanalysis. *Q. J. R. Meteorol. Soc.*, **142**, 1300-1310.

763 Jiménez, P. A., J. Dudhia, J. F. González-Rouco, J. Navarro, J. P. Montávez, and E. García-Bustamante,
764 2012: A revised scheme for the WRF surface layer formulation. *Mon. Wea. Rev.*, **140**(3), 898-
765 918.

766 [Kayaba, N., T. Yamada, S. Hayashi, K. Onogi, S. Kobayashi, K. Yoshimoto, K. Kamiguchi, and K.](#)
767 [Yamashita, 2016: Dynamical regional downscaling using the JRA-55 reanalysis \(DSJRA-55\).](#)
768 [*Sola*, **12**, pp.1-5.](#)

769 Kalnay, E., M. Kanamitsu, R. Kistler, W. Collins, D. Deaven, L. Gandin, M. Iredell, S. Saha, G. White,
770 J. Woolen, Y. Zhu, M. Chelliah, W. Ebisuzaki, W. Higgins, J. Janowiak, K. C. Mo, C. Ropelewski,
771 J. Wang, A. Leetmaa, R. Reynolds, Roy Jenne and Dennis Joseph, 1996: The NCEP/NCAR 40-
772 year reanalysis project. *Bull. Amer. Meteorol. Soc.*, **77**, 437-471.

773 Kanamitsu, M., W. Ebisuzaki, J. Woollen, S.-K. Yang, J. J. Hnilo, M. Fiorino, and G. L. Potter, 2002:
774 NCEP–DOE AMIP-II Reanalysis (R-2). *Bull. Amer. Meteor. Soc.*, **83**, 1631–1643.

775 Kay, J. K., H. M. Kim, Y.-Y. Park, and J. Son, 2013: Effect of doubling ensemble size on the

776 performance of ensemble prediction in warm season using MOGREPS implemented in
777 KMA, *Advances in Atmospheric Sciences*, **30**(5), 1287-1302, doi:10.1007/s00376-012-2083-y.
778 [Keyser, D., 2013: An Overview of Observational Data Processing at NCEP \(with information on BUFR](#)
779 [Format including “PrepBUFR” files\), *GSI tutorial*, August 6, 2013.](#)

780 Kim, S., H. M. Kim, J. K. Kay, and S.-W. Lee, 2015: Development and evaluation of high resolution
781 limited area ensemble prediction system in KMA, *Atmosphere*, 25(1), 67-83. (in Korean with
782 English abstract)

783 Kim, S., and H. M. Kim, 2017: Effect of considering sub-grid scale uncertainties on the forecasts of a
784 high-resolution limited area ensemble prediction system, *Pure and Applied Geophysics*, **174**(5),
785 2021-2037, doi: 10.1007/s00024-017-1513-2.

786 Kistler, R., W. Collins, S. Saha, G. White, J. Woollen, E. Kalnay, M. Chelliah, W. Ebisuzaki, M.
787 Kanamitsu, V. Kousky, H. v. d. Dool, R. Jenne, and M. Fiorino, 2001: The NCEP–NCAR 50–
788 Year Reanalysis: Monthly Means CD–ROM and Documentation. *Bull. Amer. Meteor. Soc.*, **82**,
789 247–267.

790 Kobayashi, S., Y. Ota, Y. Harada, A. Ebata, M. Moriya, H. Onoda, K. Onogi, H. Kamahori, C. Kobayashi,
791 H. Endo, K. Miyaoka, and K. Takahashi, 2015: The JRA-55 reanalysis: General specifications
792 and basic characteristics, *J. Meteorol. Soc. Jpn.*, **93**, 5-48.

793 Mesinger, F., G. DiMego, E. Kalnay, K. Mitchell, P. C. Shafran, W. Ebisuzaki, D. Jović, J. Woollen, E.
794 Rogers, E. H. Berbery, M. B. Ek, Y. Fan, R. Grumbine, W. Higgins, H. Li, Y. Lin, G. Manikin,
795 D. Parrish, and W. Shi, 2006: North American Regional Reanalysis. *Bull. Amer. Meteor. Soc.*,
796 **87**, 343–360.

797 Mittermaier, M. P., 2014: A strategy for verifying near-convection-resolving model forecasts at
798 observing sites. *Weather and Forecasting*, **29**(2), 185-204.

799 National Centers for Environmental Prediction/National Weather Service/NOAA/U.S. Department of
800 Commerce, 2008: NCEP ADP Global Upper Air and Surface Weather Observations
801 (PREPBUFR format). *Research Data Archive at the National Center for Atmospheric Research*,
802 *Computational and Information Systems Laboratory*, Boulder, CO. [Available online at

803 <https://doi.org/10.5065/Z83F-N512>.] Accessed 5 July 2018.

804 National Climatic Data Center/NESDIS/NOAA/U.S. Department of Commerce, Meteorology
805 Department/Florida State University, Climate Analysis Section/Climate and Global Dynamics
806 Division/National Center for Atmospheric Research/University Corporation for Atmospheric
807 Research, and Harvard College Observatory/Harvard University, 1981: World Monthly Surface
808 Station Climatology. *Research Data Archive at the National Center for Atmospheric Research,*
809 *Computational and Information Systems Laboratory*, Boulder, CO. [Available online at
810 <http://rda.ucar.edu/datasets/ds570.0/>.] Accessed 7 Nov 2019.

811 On, N., H. M. Kim, and S. Kim, 2018: Effects of resolution, cumulus parameterization scheme,
812 and probability forecasting on precipitation forecasts in a high-resolution limited-area
813 ensemble prediction system, *Asia-Pacific Journal of Atmospheric Sciences*, **54**, 623-
814 637, doi:10.1007/s13143-018-0081-4.

815 Onogi, K., J. Tsutsui, H. Koide, M. Sakamoto, S. Kobayashi, H. Hatsushika, T. Matsumoto, N.
816 Yamazaki, H. Kamahori, K. Takahashi, S. Kadokura, K. Wada, K. Kato, R. Oyama, T.
817 Ose, N. Mannoji, and R. Taira, 2007: The JRA-25 reanalysis. *J. Meteor. Soc. Japan*, **85**,
818 369–432.

819 Park, J., and H. M. Kim, 2020: Design and evaluation of CO₂ observation network to optimize surface
820 CO₂ fluxes in Asia using observation system simulation experiments, *Atmospheric Chemistry*
821 *and Physics*, **20**, 5175-5195, <https://doi.org/10.5194/acp-20-5175-2020>.

822 Penny, S. G., 2014: The hybrid local ensemble transform Kalman filter. *Monthly Weather Review*,
823 **142**(6), 2139-2149.

824 Penny, S. G., D. W. Behringer, J. A. Carton, and E. Kalnay, 2015: A hybrid global ocean data
825 assimilation system at NCEP. *Monthly Weather Review*, **143**(11), 4660-4677.

826 Que, L. J., W. L. Que, and J. M. Feng, 2016: Intercomparison of different physics schemes in the WRF
827 model over the Asian summer monsoon region. *Atmospheric and Oceanic Science Letters*, **9**(3),
828 169-177.

829 Renshaw, R., P. Jermey, D. Barker, A. Maycock, and S. Oxley, 2013: EURO4M regional reanalysis
830 system, *Forecasting Research Technical Report*, No. **583**, Met Office.

831 Rienecker, M. M., M. J. Suarez, R. Gelaro, R. Todling, J. Bacmeister, E. Liu, M. G. Bosilovich, S. D.
832 Schubert, L. Takacs, G.-K. Kim, S. Bloom, J. Chen, D. Collins, A. Conaty, A. da Silva, W. Gu,
833 J. Joiner, R. D. Koster, R. Lucchesi, A. Molod, T. Owens, S. Pawson, P. Pegion, C. R. Redder,
834 R. Reichle, F. R. Robertson, A. G. Ruddick, M. Sienkiewicz, and J. Woollen, 2011: MERRA:
835 NASA's Modern-Era Retrospective Analysis for Research and Applications. *J. Climate*, **24**,
836 3624–3648.

837 Saha, S., S. Moorthi, H.-L. Pan, X. Wu, J. Wang, S. Nadiga, P. Tripp, R. Kistler, J. Woollen, D. Behringer,
838 H. Liu, D. Stokes, R. Grumbine, G. Gayno, J. Wang, Y.-T. Hou, H.-Y. Chuang, H.-M. H. Juang,
839 J. Sela, M. Iredell, R. Treadon, D. Kleist, P. V. Delst, D. Keyser, J. Derber, M. Ek, J. Meng, H.
840 Wei, R. Yang, S. Lord, H. V. D. Dool, A. Kumar, W. Wang, C. Long, M. Chelliah, Y. Xue, B.
841 Huang, J.-K. Schemm, W. Ebisuzaki, R. Lin, P. Xie, M. Chen, S. Zhou, W. Higgins, C.-Z. Zou,
842 Q. Liu, Y. Chen, Y. Han, L. Cucurull, R. W. Reynolds, G. Rutledge, and M. Goldberg, 2010: The
843 NCEP Climate Forecast System Reanalysis. *Bull. Amer. Meteor. Soc.*, **91**, 1015–1057.

844 Schubert, S., J. Pfendtner, and R. Rood, 1993: An assimilated dataset for earth science applications.
845 *Bull. Amer. Meteor. Soc.*, **74**, 2331–2342.

846 Shiferaw, A., T. Tadesse, C. Rowe, and R. Oglesby, 2018: Precipitation extremes in dynamically
847 downscaled climate scenarios over the greater horn of Africa. *Atmosphere*, **9**(3), 112.

848 Shin, I.-C, J.-G. Kim, C.-Y. Chung, S.-K. Baek, and J.-R. Lee, 2016: The impact of the COMS data on
849 the KMA NWP System, *14th JCSDA Technical Review Meeting & Science Workshop on*
850 *Satellite Data Assimilation*.

851 Skamarock, W. C., J. B. Klemp, J. Dudhia, D. O. Gill, D. M. Barker, M. G. Duda, X.-Y. Huang, W.
852 Wang, J. G. Powers, 2008: A description of the advanced research WRF version 3. NCAR Tech.
853 Note NCAR/TN-475+ STR Available at:
854 <https://opensky.ucar.edu/islandora/object/technotes%3A500/datastream/PDF/view>.

855 Tewari, M., F. Chen, W. Wang, J. Dudhia, M. A. LeMone, K. Mitchell, M. Ek, G. Gayno, J. Wegiel, and

856 R. H. Cuenca, 2004: Implementation and verification of the unified NOAH land surface model
857 in the WRF model. *20th conference on weather analysis and forecasting/16th conference on*
858 *numerical weather prediction* (Vol. 1115). Seattle, WA: American Meteorological Society.

859 Theis, S. E., A. Hense, and U. Damrath, 2005: Probabilistic precipitation forecasts from a deterministic
860 model: A pragmatic approach. *Meteorological Applications: A journal of forecasting, practical*
861 *applications, training techniques and modelling*, **12**(3), 257-268.

862 Thompson, G., P. R. Field, R. M. Rasmussen, and W. D. Hall, 2008: Explicit forecasts of winter
863 precipitation using an improved bulk microphysics scheme. Part II: Implementation of a new
864 snow parameterization. *Mon. Wea. Rev.*, **136**(12), 5095-5115.

865 Uppala, S. M., P. W. Kållberg, A. J. Simmons, U. Andrae, V. D. C. Bechtold, M. Fiorino, J. K. Gibson,
866 J. Haseler, A. Hernandez, G. A. Kelly, X. Li, K. Onogi, S. Saarinen, N. Sokka, R. P. Allan, E.
867 Andersson, K. Arpe, M. A. Balmaseda, A. C. M. Beljaars, L. V. D. Berg, J. Bidlot, N. Bormann,
868 S. Caires, F. Chevallier, A. Dethof, M. Dragosavac, M. Fisher, M. Fuentes, S. Hagemann, E.
869 Hólm, B. J. Hoskins, L. Isaksen, P. A. E. M. Janssen, R. Jenne, A. P. McNally, J.-F. Mahfouf, J.-
870 J. Morcrette, N. A. Rayner, R. W. Saunders, P. Simon, A. Sterl, K. E. Trenberth, A. Untch, D.
871 Vasiljevic, P. Viterbo, and J. Woollen, 2005: The ERA-40 re-analysis. *Q. J. R. Meteorol. Soc.*,
872 **131**: 2961–3012.

873 Warrick, F., 2015: Options for filling the LEO-GEO AMV Coverage Gap. *NWP SAF Tech. Doc.*, NWP
874 SAF-MO-TR-030, 21 p.

875 Wilks, D. S., 2006: Statistical methods in the atmospheric sciences, 2nd edn., *Academic Press*, 627pp.

876 Wilson, L., 2010: Verification of severe weather forecasts in support of the “SWFDP Southern Africa”
877 project. *Report for the World Meteorological Organisation*, pp. 21
878 (www.wmo.int/pages/prog/www/BAS/documents/Doc-7-Verification.doc)

879 Yang, E.-G., and H. M. Kim, 2017: Evaluation of a regional reanalysis and ERA-Interim over East Asia
880 using in situ observations during 2013-14, *Journal of Applied Meteorology and*
881 *Climatology*, **56**(10), 2821-2844,

882 Yang, E.-G., and H. M. Kim, 2019: Evaluation of Short-Range Precipitation Reforecasts from East Asia

883 Regional Reanalysis. *Journal of Hydrometeorology*, **20**(2), 319-337.

884 Yang, E.-G., and H. M. Kim, 2021a: A comparison of variational, ensemble-based, and hybrid data
885 assimilation methods over East Asia for two one-month periods, *Atmospheric Research*, **249**,
886 105257.

887 Yang, E.-G., and H. M. Kim, 2021b: East Asia Regional Reanalysis 6 hourly data on pressure levels
888 from 2010 to 2019, <https://doi.org/10.7910/DVN/7P8MZT>, Harvard Dataverse, V1.

889 Yang, E.-G., and H. M. Kim, 2021c: East Asia Regional Reanalysis 6 hourly precipitation data from
890 2010 to 2019, <https://doi.org/10.7910/DVN/Q07VRC>, Harvard Dataverse, V1.

891 Yoo, C., and E. Cho, 2018: Comparison of GCM precipitation predictions with their RMSEs and pattern
892 correlation coefficients. *Water*, **10**(1), 28.

893 Zhang, F., M. Zhang, and J. Poterjoy, 2013: E3DVar: Coupling an ensemble Kalman filter with three-
894 dimensional variational data assimilation in a limited-area weather prediction model and
895 comparison to E4DVar. *Monthly Weather Review*, **141**(3), 900-917.

896 Zhang, Q., Y. Pan, S. Wang, J. Xu, and J. Tang, 2017: High-resolution regional reanalysis in China:
897 Evaluation of 1 year period experiments. *Journal of Geophysical Research: Atmospheres*,
898 **122**(20), 10-801.

899

900 **Table caption**

901 Table 1. Model configuration.

902 Table 2. Summary of observations used in this study. The default observation error statistics
903 provided in WRFDA system are used for assimilation in this study. The variables u, v, T, RH,
904 Ps, and TPW denote zonal wind, meridional wind, temperature, relative humidity, surface
905 pressure, and total precipitable water, respectively.

906 Table 3. (Re)analyses and (re)forecasts and corresponding experiments used in this study.

907 Table 24. The 2×2 contingency table for dichotomous (yes-no) events.

908

909 **Figure caption**

910 ~~Figure 1. The model domain over East Asia with verification area (black dashed box).~~

911 Figure 1. The East Asia Regional Reanalysis domain with different types of NCEP PrepBUFR
912 observations available for assimilation at 00 UTC on 1st of January in 2017. The black dashed
913 box denotes a verification area.

914 Figure 2. The schematic diagram of the advanced hybrid gain data assimilation method in the
915 East Asia regional reanalysis system.

916 Figure 23. RMSEs of analysis of (a,b) zonal wind, (c,d) meridional wind, (e,f) temperature,
917 and (g,h) Qvapor (water vapor mixing ratio) from ERA-I (black dashed), ERA5 (black solid),
918 E3DVAR (blue dashed), AdvHG (blue solid) depending on pressure levels for (left) January
919 and (right) July in 2017.

920 Figure 34. Same as Fig. 23 except for 24 h forecast.

921 Figure 45. Same as Fig. 23 except for 36 h forecast.

922 Figure 56. RMSEs of analysis of (a) zonal wind, (b) meridional wind, (c) temperature, and (d)
923 Qvapor (water vapor mixing ratio) from ERA5 (black solid) and AdvHG (blue solid) and
924 spreads of analysis (black dashed) and 6 h forecast (gray dashed) of AdvHG depending on
925 pressure levels averaged over the two-year period of 2017–2018.

926 Figure 67. Same as Fig. 56 except for RMSE of 24 h forecast.

927 Figure 78. (a,c) ETS and (b,d) FBI for (a,b) January and (c,d) July in 2017 depending on
928 thresholds 0.5, 1, 4, 8, and 16 mm (6 h)⁻¹.

929 Figure 89. (a,c) POD and (b,d) FAR for (a,b) January and (c,d) July in 2017 depending on
930 thresholds 0.5, 1, 4, 8, and 16 mm (6 h)⁻¹.

931 Figure [910](#). Brier skill score of the probabilistic postprocessed forecast with reference to the
932 WRF-based ERA-I for (a-d) January and (e-h) July in 2017 (Blue solid: AdvHG, blue dashed:
933 E3DVAR, red solid: WRF-based ERA5).

934 Figure [1011](#). The spatial distribution of 6 h accumulated precipitation of (1st column)
935 observation, (2nd column) E3DVAR, (3rd column) AdvHG, (4th column) ERA-I, (5th column)
936 ERA5, (6th column) ERA-I_fromECMWF, and (7th column) ERA5_fromECMWF and the
937 pattern correlation coefficient (PCC) shown at the bottom right of each figure at valid time (1st
938 low, 3rd low) 06 UTC and (2nd low, 4th low) 18 UTC on 29th and 30th of January in 2017.

939 Figure [1112](#). As in Fig. [1011](#), but for 1st and 2nd of July in 2017.

940 Figure [1213](#). The spatial distribution of the monthly accumulated precipitation of (a)
941 observations, (b) E3DVAR, (c) AdvHG, (d) ERA-I, (e) ERA5, (f) ERA-I from ECMWF, and
942 (g) ERA5 from ECMWF for January 2017.

943 Figure [1314](#). As in Fig. [1213](#), but for July 2017.

944

945 Table 1. Model configuration

	Description
Hori. Resol.	12 km (540×432 grid points)
Vert. Lev.	50 vertical levels (up to 5 hPa)
Model	WRF Model (v3.7.1, Skamarock et al. 2008)
LBC	ERA5 (Hersbach et al. 2020)
Data assimilation	E3DVAR (Zhang et al. 2013), Adanced hybrid gain method
Microphysics	Thompson scheme (Thompson et al. 2008)
Cumulus convection	Grell–Freitas ensemble scheme (Grell and Freitas 2014)
PBL	Yonsei University scheme (Hong et al. 2006)
Radiation	Rapid Radiative Transfer Model (RRTMG) scheme (Iacono et al. 2008)
Surface layer	Revised MM5 Monin-Obukhov scheme (Jiménez et al. 2012)
Surface model	Unified Noah Land Surface Model (Tewari et al. 2004)

946

947

948 Table 2. Summary of observations used in this study. The default observation error statistics
 949 provided in WRFDA system are used for assimilation in this study. The variables u, v, T, RH,
 950 Ps, and TPW denote zonal wind, meridional wind, temperature, relative humidity, surface
 951 pressure, and total precipitable water, respectively.

<u>Observations</u>	<u>Descriptions</u>	<u>Variables</u>	<u>Observation errors</u> <u>(depending on vertical</u> <u>levels)</u>
<u>SOUND</u>	<u>Upper-air observation from radiosonde</u>	<u>u, v</u>	<u>1.1-3.3 m/s</u>
		<u>T</u>	<u>1 K</u>
		<u>RH</u>	<u>10-15%</u>
<u>PROFILER</u>	<u>Upper-air wind profile from wind profiler</u>	<u>u, v</u>	<u>2.2-3.2 m/s</u>
<u>PILOT</u>	<u>Upper-air wind profile from pilot balloon or</u> <u>radiosonde</u>	<u>u, v</u>	<u>2.2-3.2 m/s</u>
<u>AIREP</u>	<u>Upper-air wind and temperature from aircraft</u>	<u>u, v</u>	<u>3.6 m/s</u>
		<u>T</u>	<u>1 K</u>
<u>Scatwind</u>	<u>Scatterometer oceanic surface winds</u>	<u>u, v</u>	<u>2.5-3.8 m/s</u>
<u>SHIPS</u>	<u>Surface synoptic observation from ship</u>	<u>u, v</u>	<u>1.1 m/s</u>
		<u>T</u>	<u>2 K</u>
		<u>Ps</u>	<u>1.6 hPa</u>
		<u>RH</u>	<u>10%</u>
<u>SYNOP</u>	<u>Surface synoptic observation from land station</u>	<u>u, v</u>	<u>1.1 m/s</u>
		<u>T</u>	<u>2 K</u>
		<u>Ps</u>	<u>1 hPa</u>
		<u>RH</u>	<u>10%</u>
<u>BUOY</u>	<u>Surface synoptic observation from buoy</u>	<u>u, v</u>	<u>1.4-1.6 m/s</u>
		<u>T</u>	<u>2 K</u>
		<u>Ps</u>	<u>0.9-1 hPa</u>
		<u>RH</u>	<u>10%</u>
<u>GPSPW</u>	<u>Precipitable water vapor from global positioning</u> <u>system (GPS)</u>	<u>TPW</u>	<u>0.2 mm</u>
<u>METAR</u>	<u>Aviation routine weather report from automatic</u> <u>weather station (AWS)</u>	<u>u, v</u>	<u>1.1 m/s</u>
		<u>T</u>	<u>2 K</u>
		<u>Ps</u>	<u>1 hPa</u>
		<u>RH</u>	<u>10%</u>
<u>AMV</u>	<u>Conventional atmospheric motion vector data</u> <u>from geostationary satellite</u>	<u>u, v</u>	<u>2.5-4.5 m/s</u>

952

953

954

955 Table 3. (Re)analyses and (re)forecasts and corresponding experiments used in this study.

<u>Experiment</u>	<u>(Re)analysis</u>	<u>(Re)forecast</u>
<u>AdvHG (EARR)</u>	<u>Reanalysis from AdvHG</u>	<u>Generated using WRF</u>
<u>E3DVAR</u>	<u>Analysis from E3DVAR</u>	<u>Generated using WRF</u>
<u>WRF-based ERA5</u>	<u>Reanalysis from ERA5</u>	<u>Generated using WRF</u>
<u>WRF-based ERA-I</u>	<u>Reanalysis from ERA-I</u>	<u>Generated using WRF</u>
<u>ERA5_fromECMWF</u>	<u>Reanalysis from ERA5</u>	<u>Downloaded from ECMWF</u>
<u>ERA-I_fromECMWF</u>	<u>Reanalysis from ERA-I</u>	<u>Downloaded from ECMWF</u>

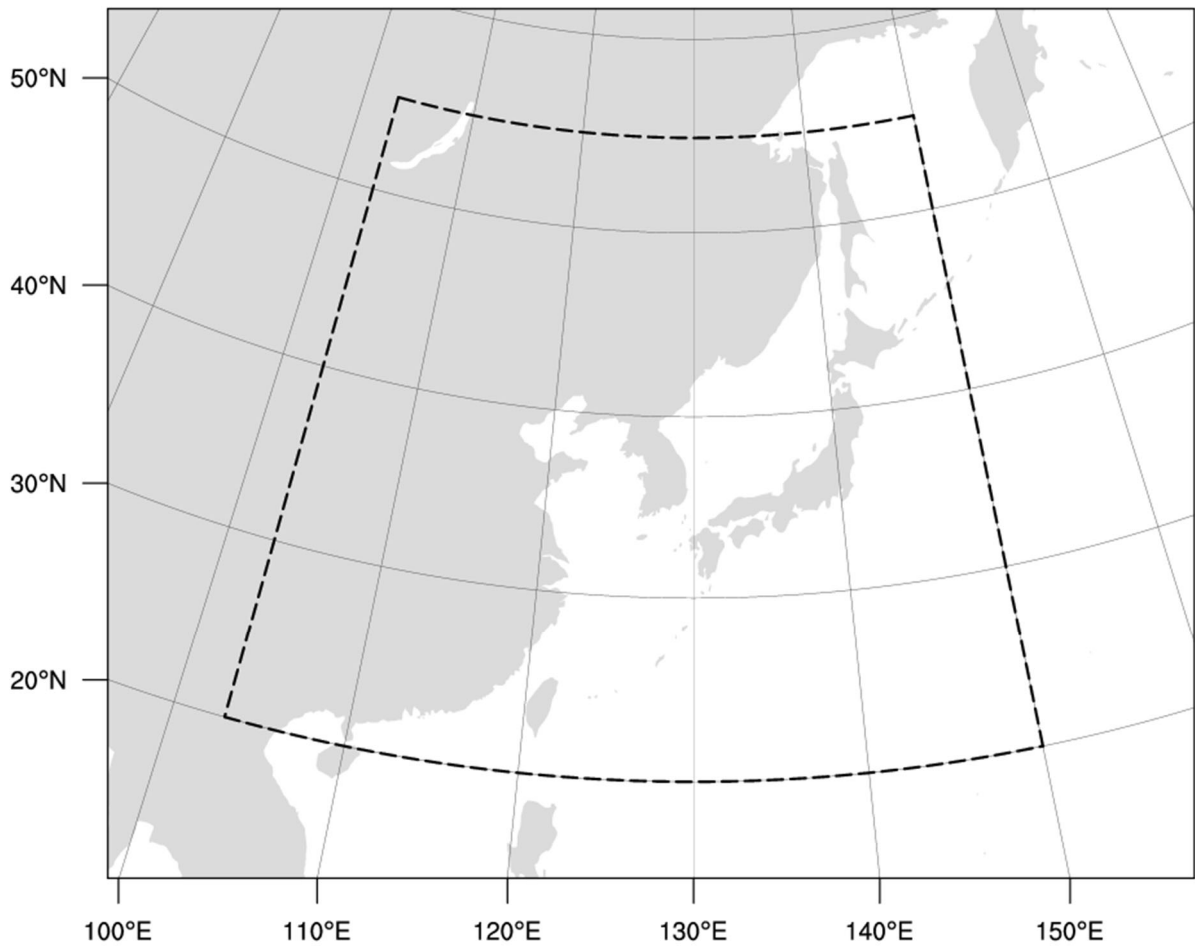
956

957 Table 24. The 2×2 contingency table for dichotomous (yes-no) events.

Forecast	Observed		
	Yes	No	
Yes	Hits (A)	False alarms (B)	A + B
No	Misses (C)	Correct rejections (D)	C + D
	A + C	B + D	Total = A + B + C + D

958

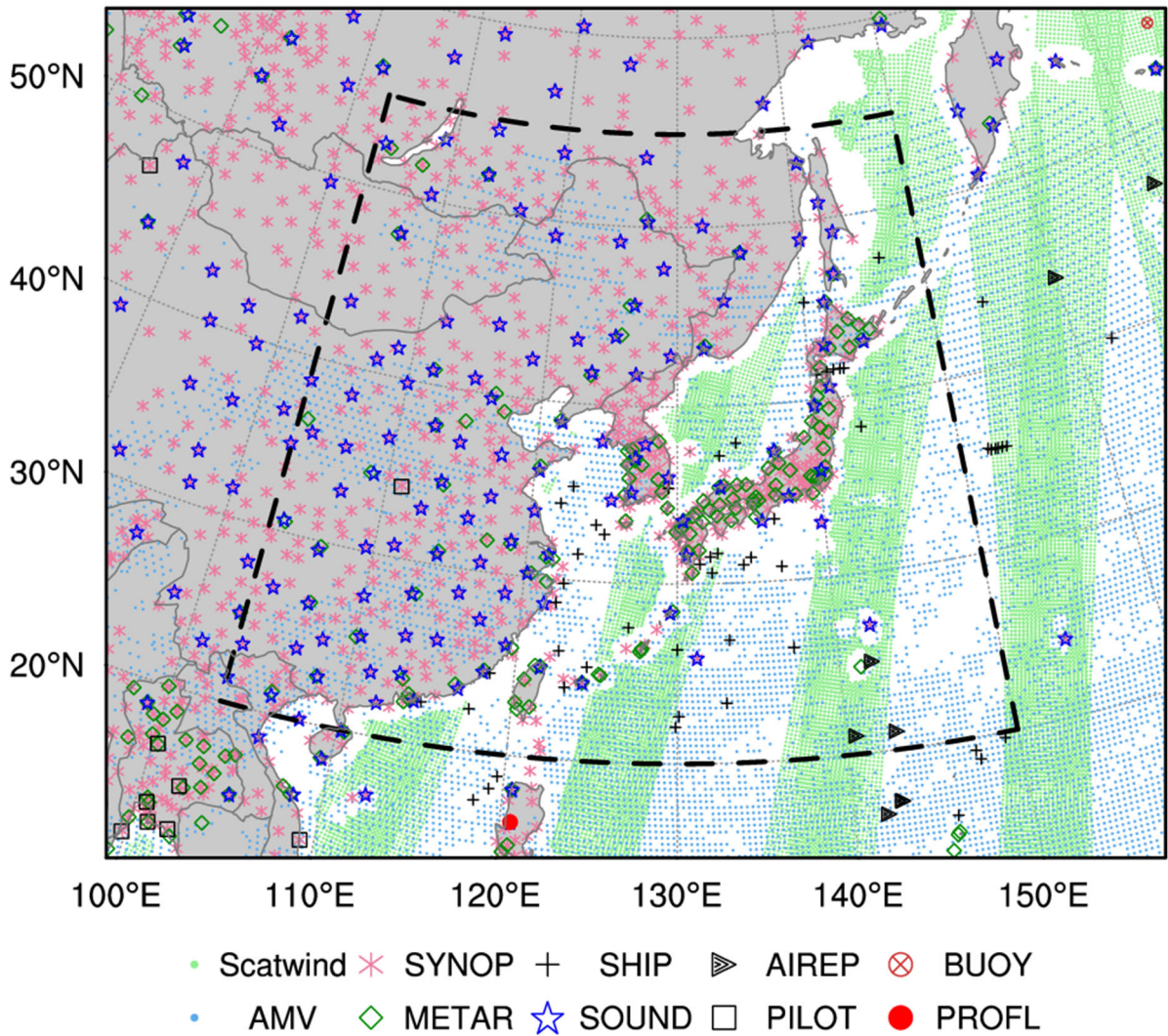
959



960

961

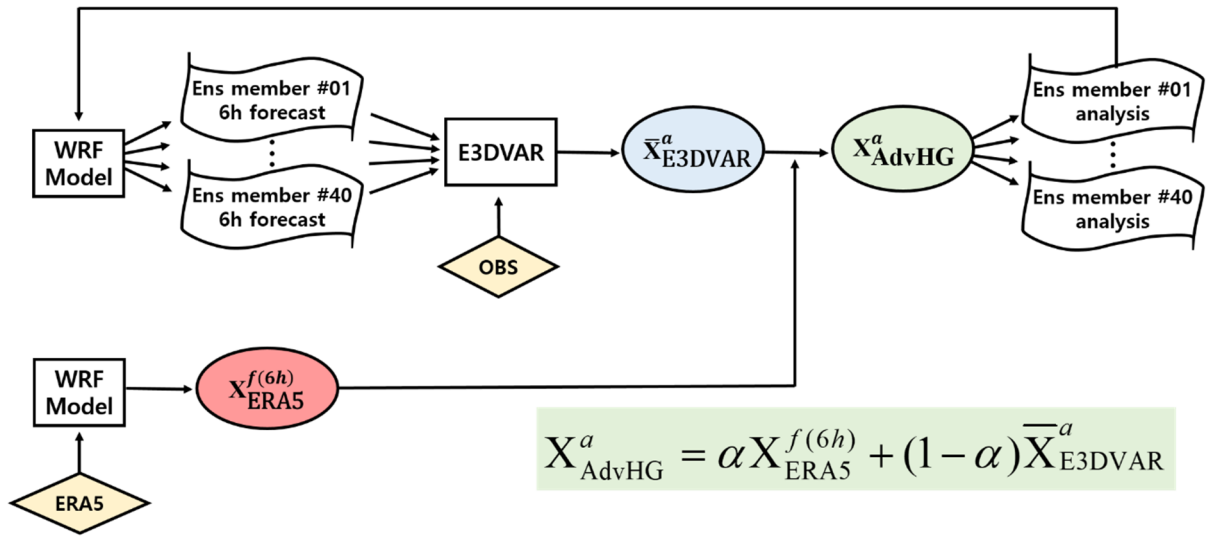
Figure 1. The model domain over East Asia with verification area (black dashed box).



962

963 Figure 1. The East Asia Regional Reanalysis domain with different types of NCEP PrepBUFR
 964 observations available for assimilation at 00 UTC on 1st of January in 2017. The black dashed
 965 box denotes a verification area.

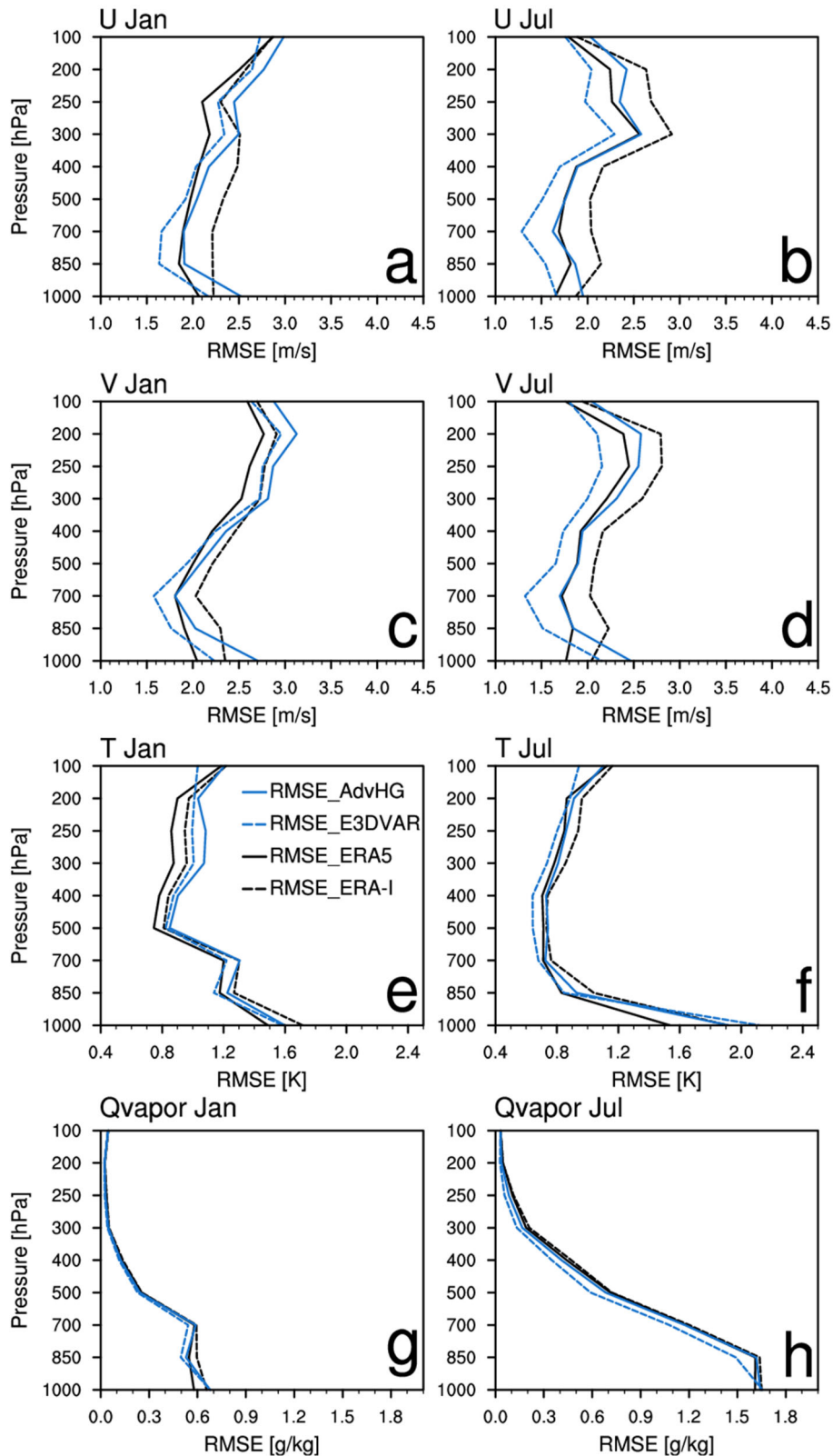
966



967

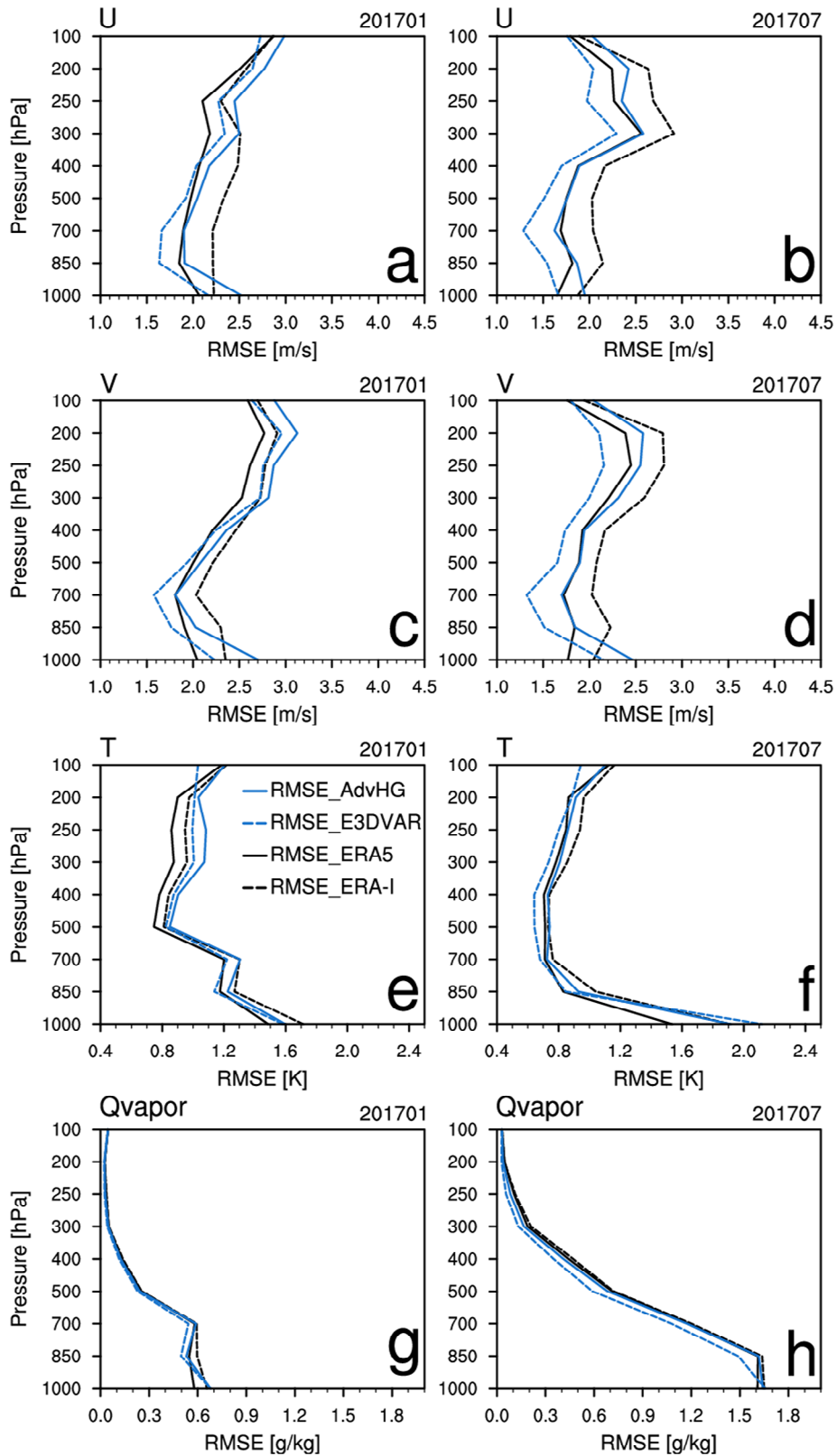
968 Figure 2. The schematic diagram of the advanced hybrid gain data assimilation method in the
 969 East Asia regional reanalysis system.

970



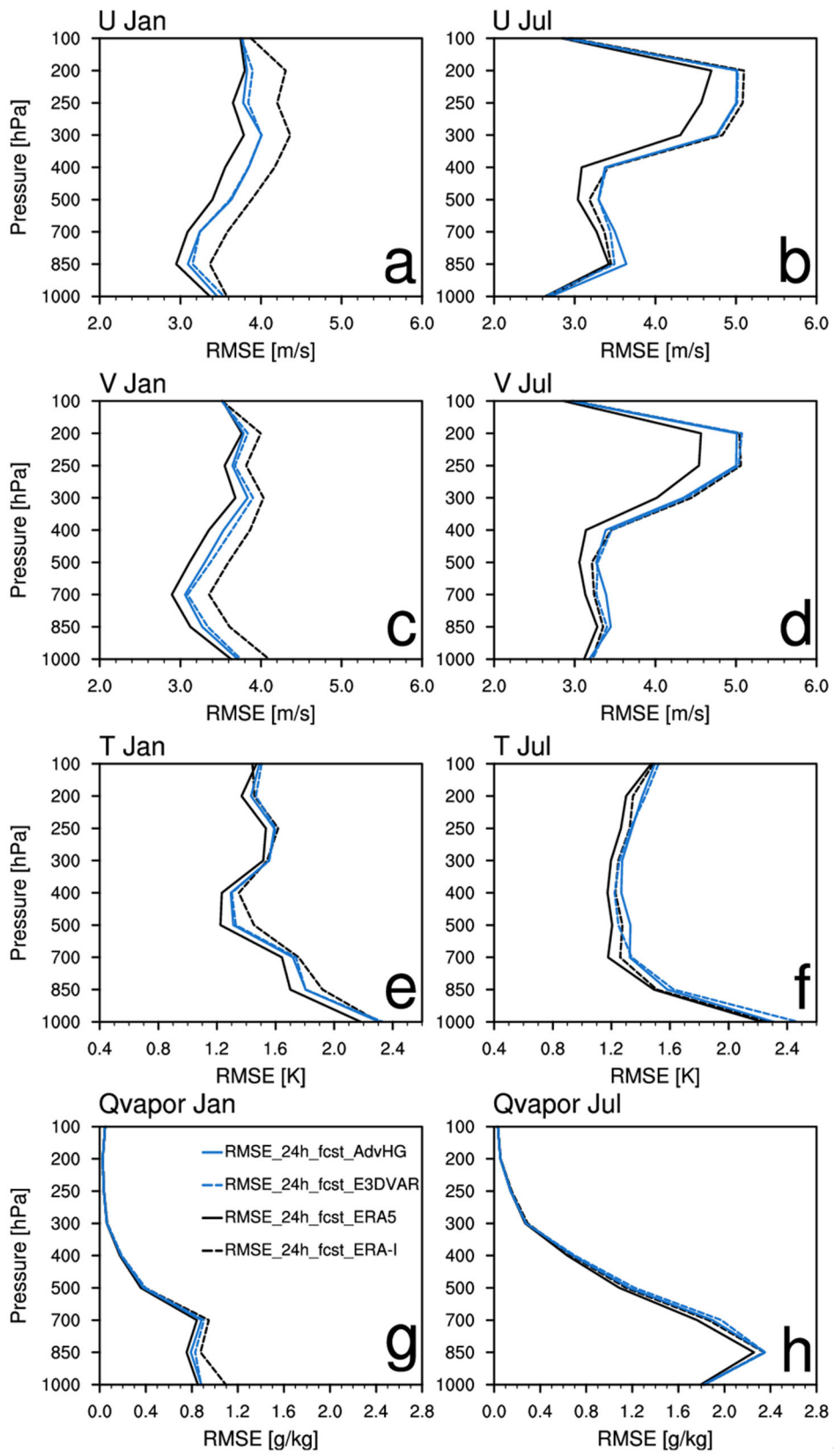
971

972 **Figure 2. RMSEs of analysis of (a,b) zonal wind, (c,d) meridional wind, (e,f) temperature, and**
 973 **(g,h) Qvapor (water vapor mixing ratio) from ERA-I (black dashed), ERA5 (black solid),**
 974 **E3DVAR (blue dashed), AdvHG (blue solid) depending on pressure levels for (left) January**
 975 **and (right) July in 2017.**



976

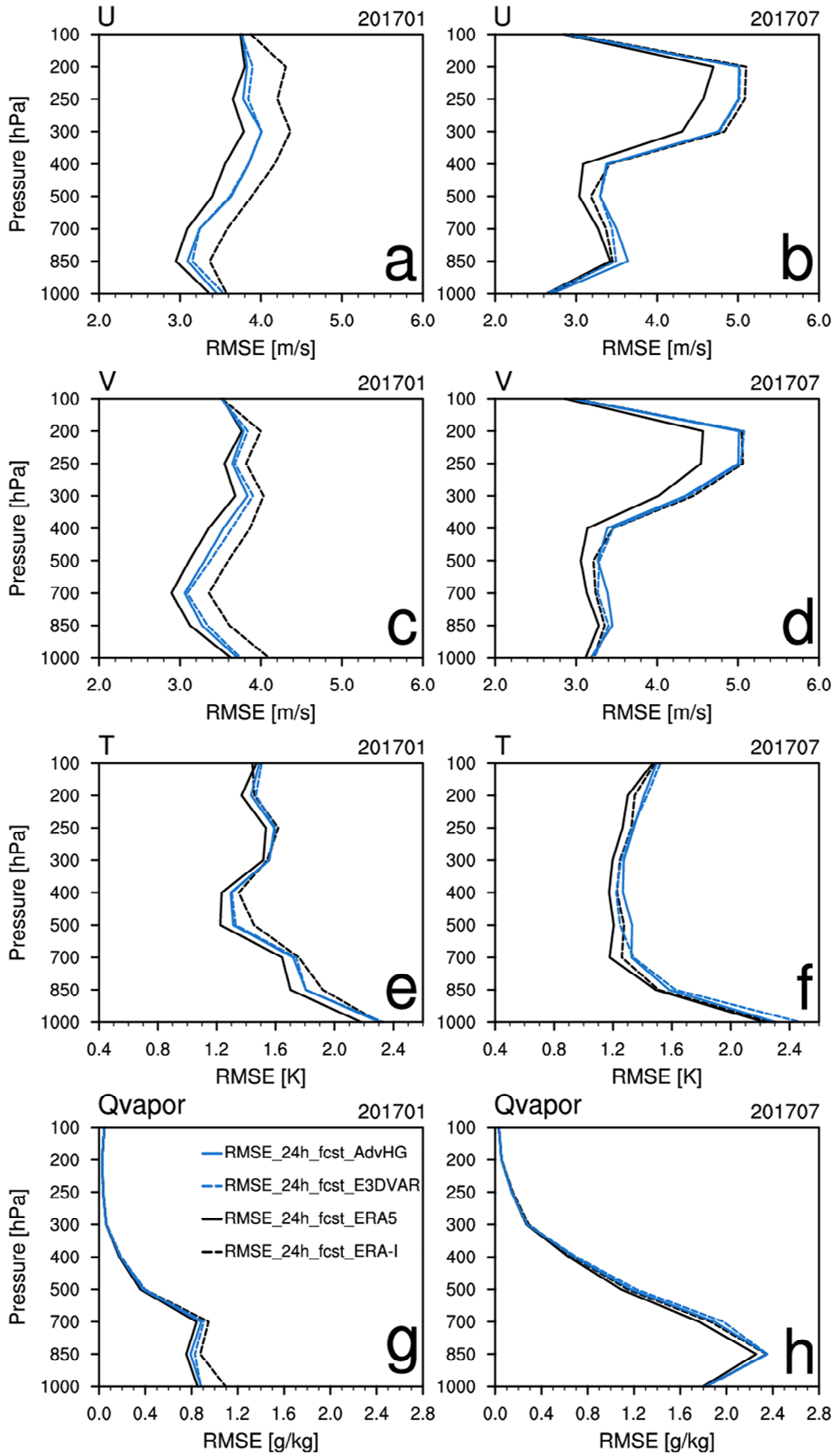
977 Figure 3. RMSEs of analysis of (a,b) zonal wind, (c,d) meridional wind, (e,f) temperature, and
 978 (g,h) Qvapor (water vapor mixing ratio) from ERA-I (black dashed), ERA5 (black solid),
 979 E3DVAR (blue dashed), AdvHG (blue solid) depending on pressure levels for (left) January
 980 and (right) July in 2017.



981

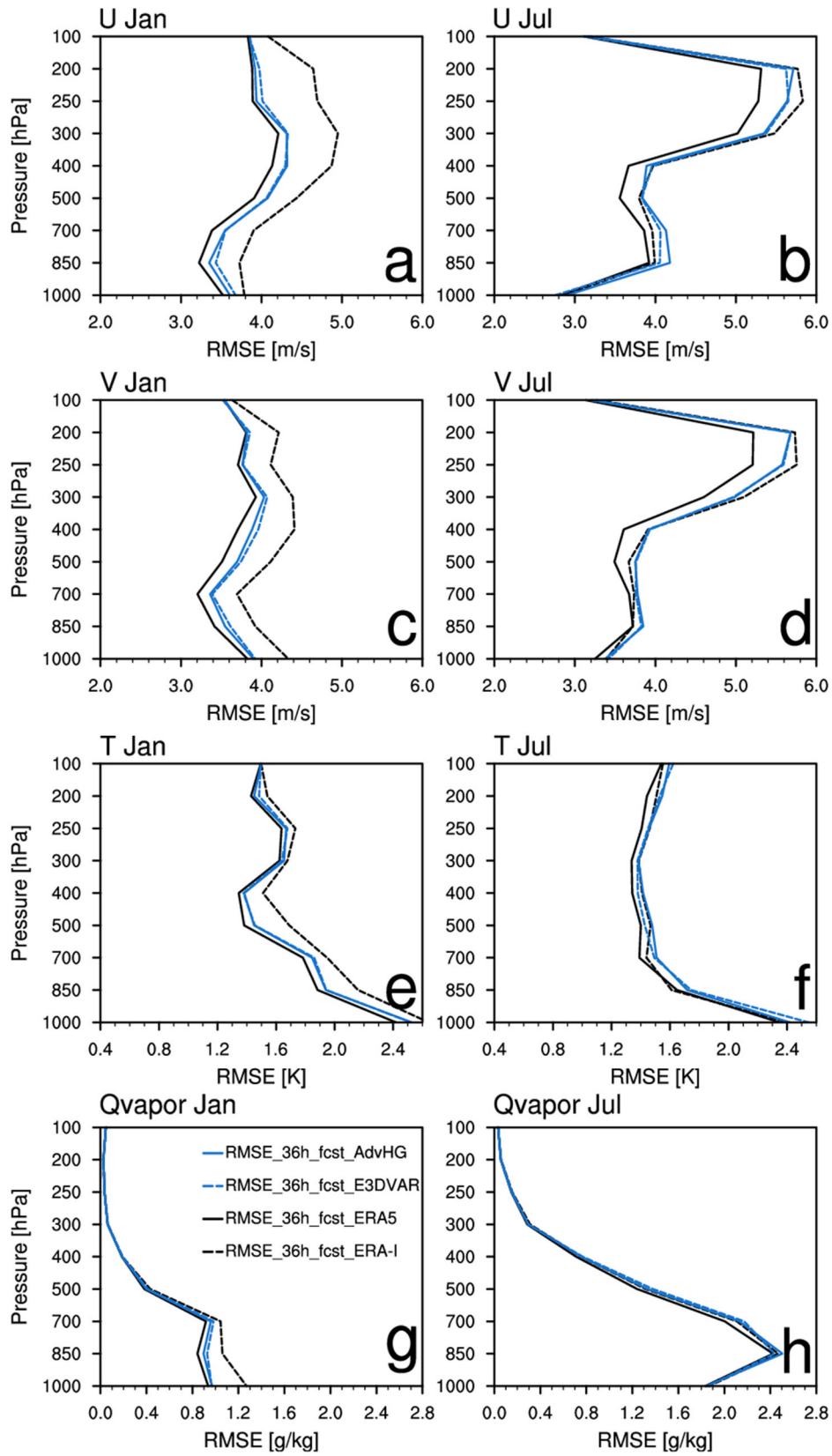
982

Figure 3. Same as Fig. 2 except for 24 h forecast.



983

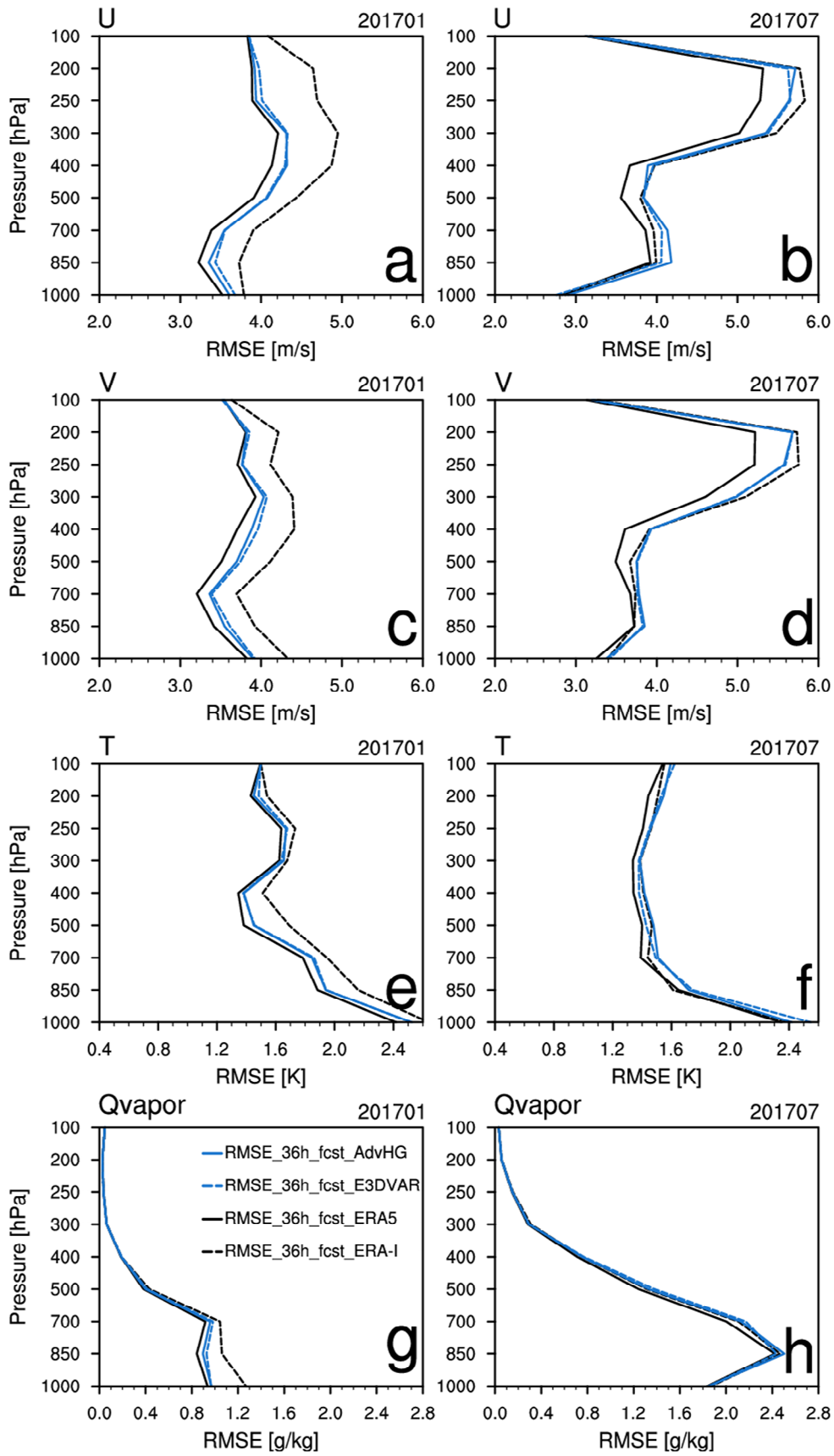
984 Figure 4. Same as Fig. 3 except for 24 h forecast.



985

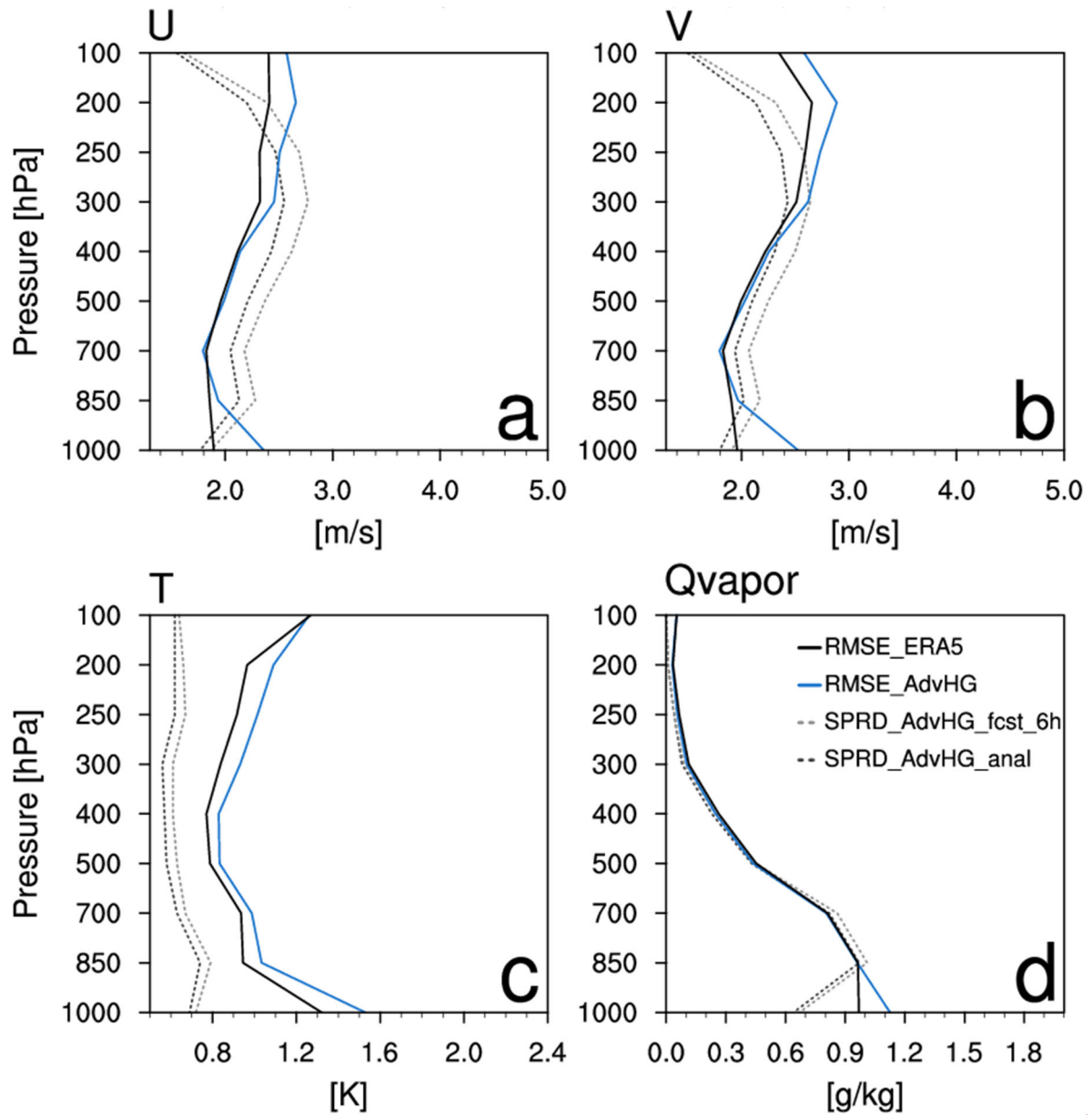
986

Figure 4. Same as Fig. 2 except for 36 h forecast.



987

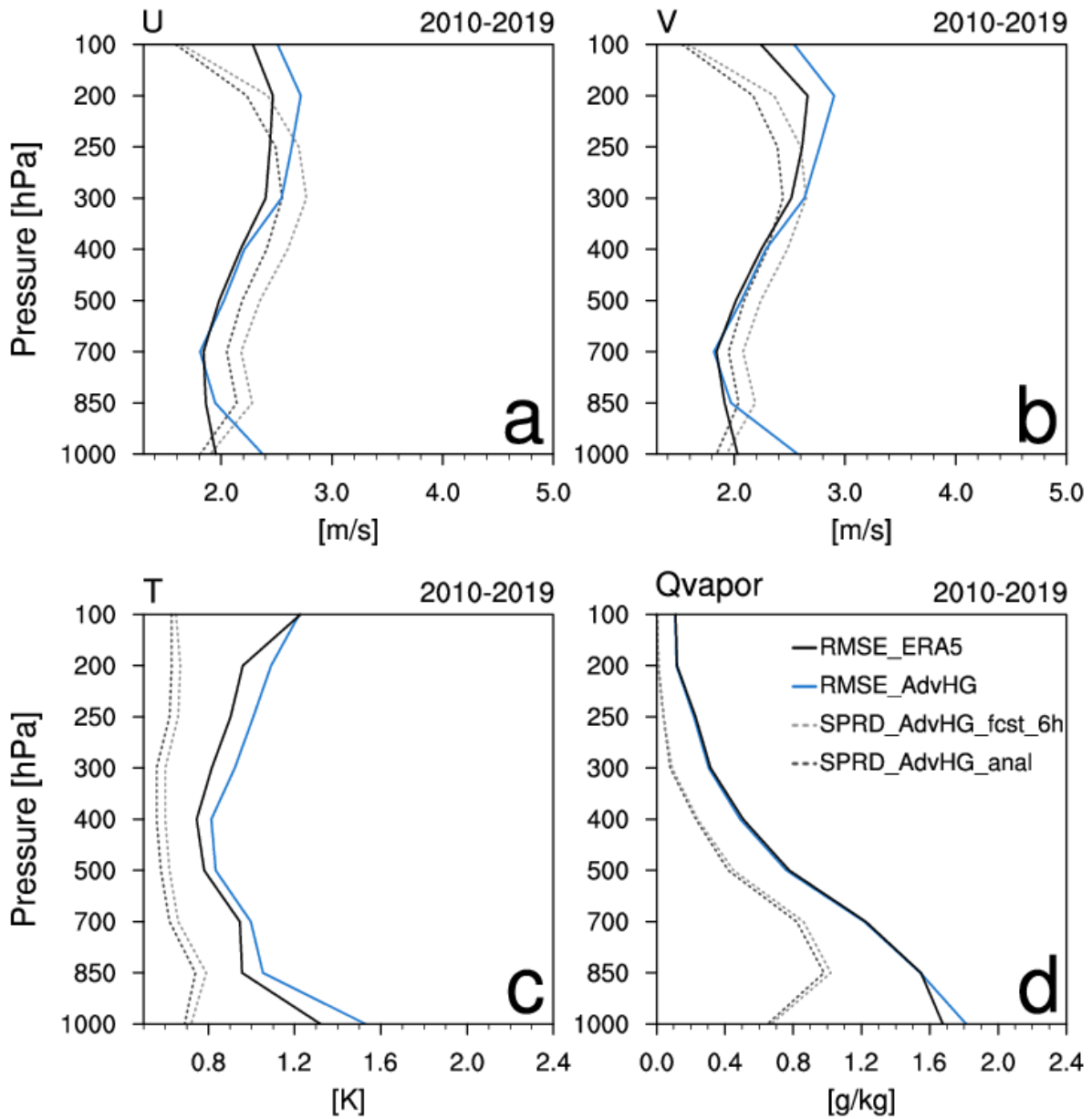
988 Figure 5. Same as Fig. 3 except for 36 h forecast.



989

990 **Figure 5. RMSEs of analysis of (a) zonal wind, (b) meridional wind, (c) temperature, and (d)**
 991 **Qvapor (water vapor mixing ratio) from ERA5 (black solid) and AdvHG (blue solid) and**
 992 **spreads of analysis (black dashed) and 6 h forecast (gray dashed) of AdvHG depending on**
 993 **pressure levels averaged over the two-year period of 2017–2018.**

994



995

996 Figure 6. RMSEs of analysis of (a) zonal wind, (b) meridional wind, (c) temperature, and (d)
 997 Qvapor (water vapor mixing ratio) from ERA5 (black solid) and AdvHG (blue solid) and
 998 spreads of analysis (black dashed) and 6 h forecast (gray dashed) of AdvHG depending on
 999 pressure levels averaged over the ten-year period of 2010–2019.

1000

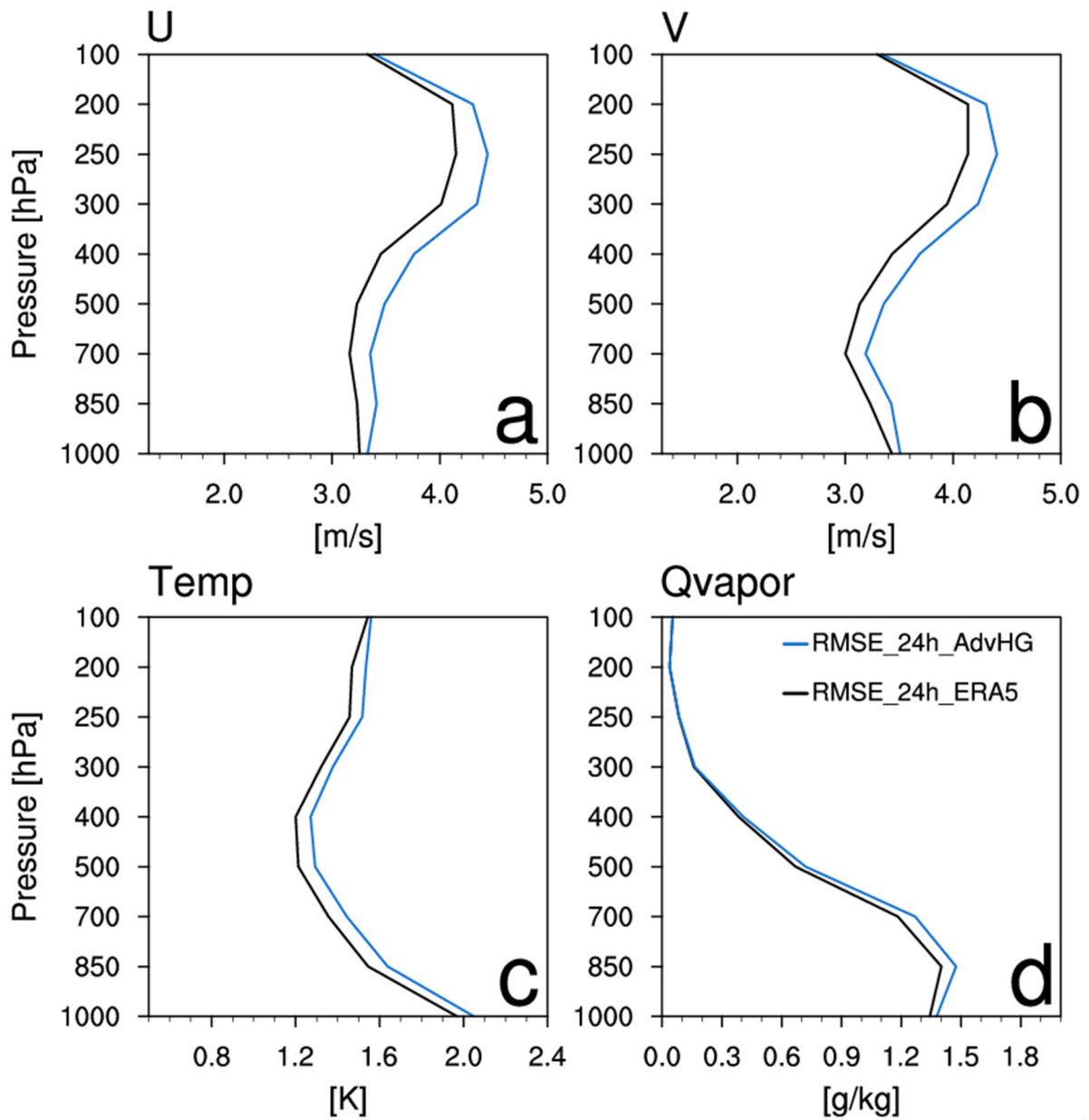


Figure 6. Same as Fig. 5 except for RMSE of 24 h forecast.

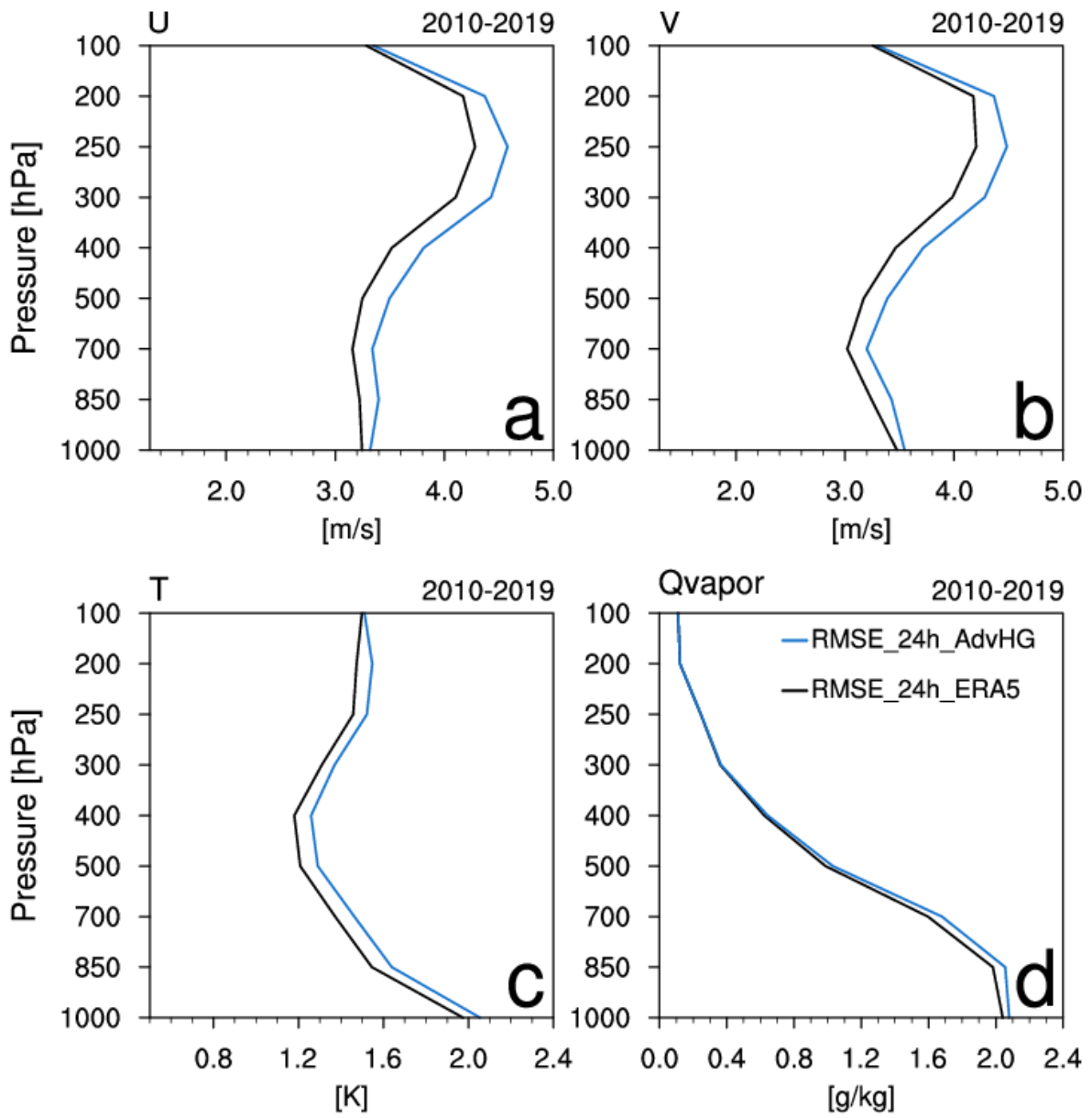
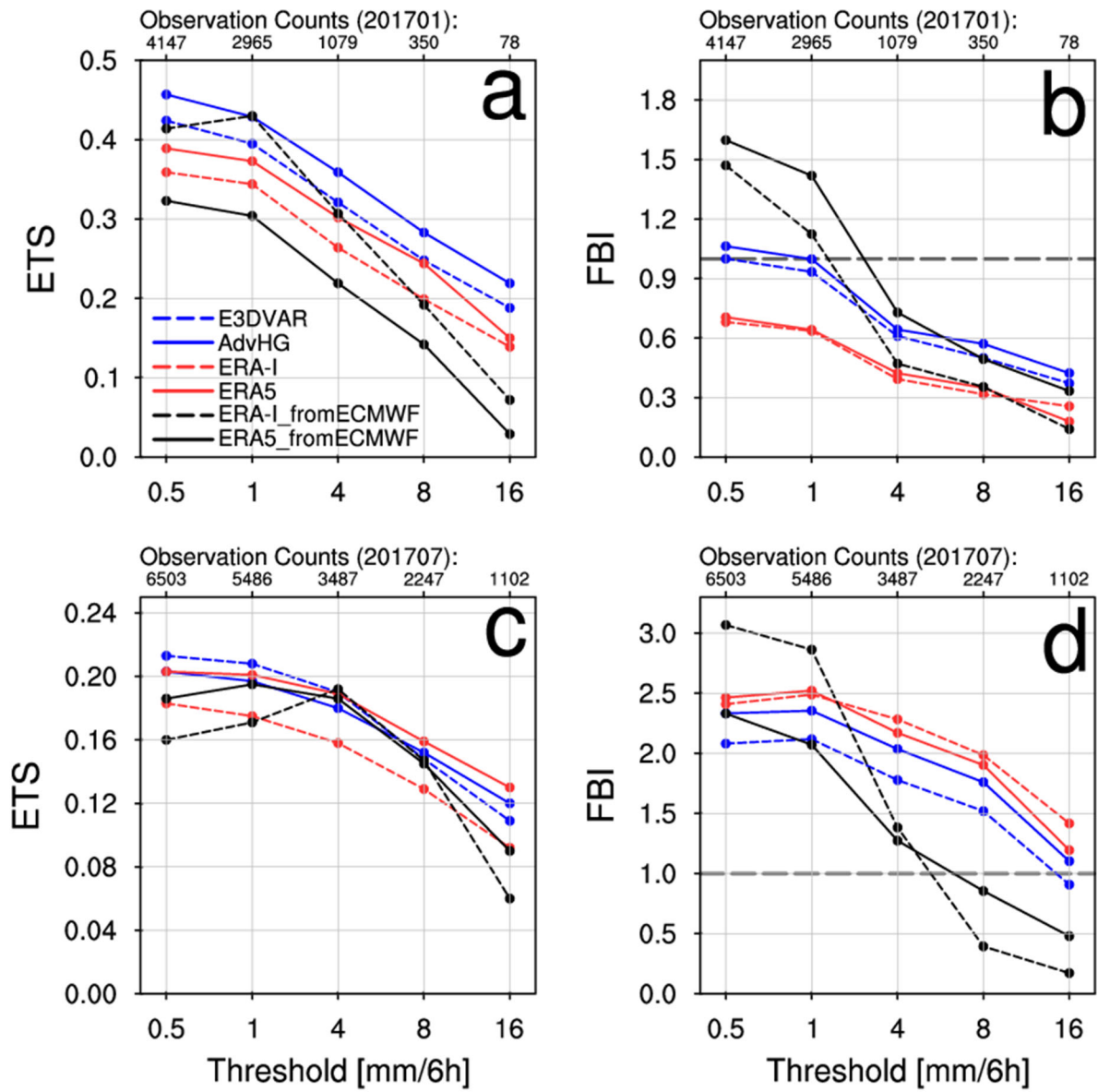


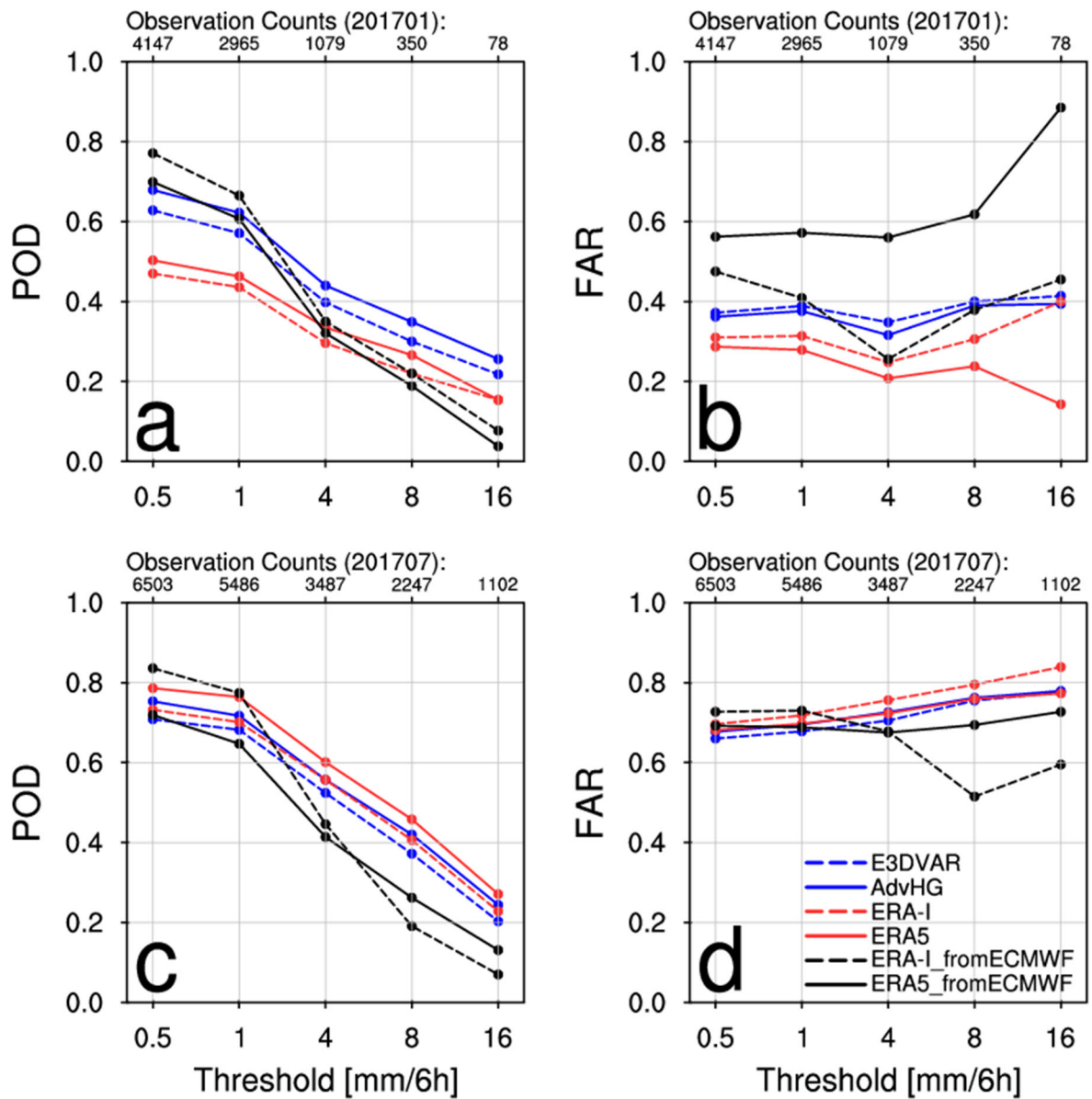
Figure 7. Same as Fig. 6 except for RMSE of 24 h forecast.



1007

1008 Figure 78. (a,c) ETS and (b,d) FBI for (a,b) January and (c,d) July in 2017 depending on
 1009 thresholds 0.5, 1, 4, 8, and 16 mm (6 h)⁻¹.

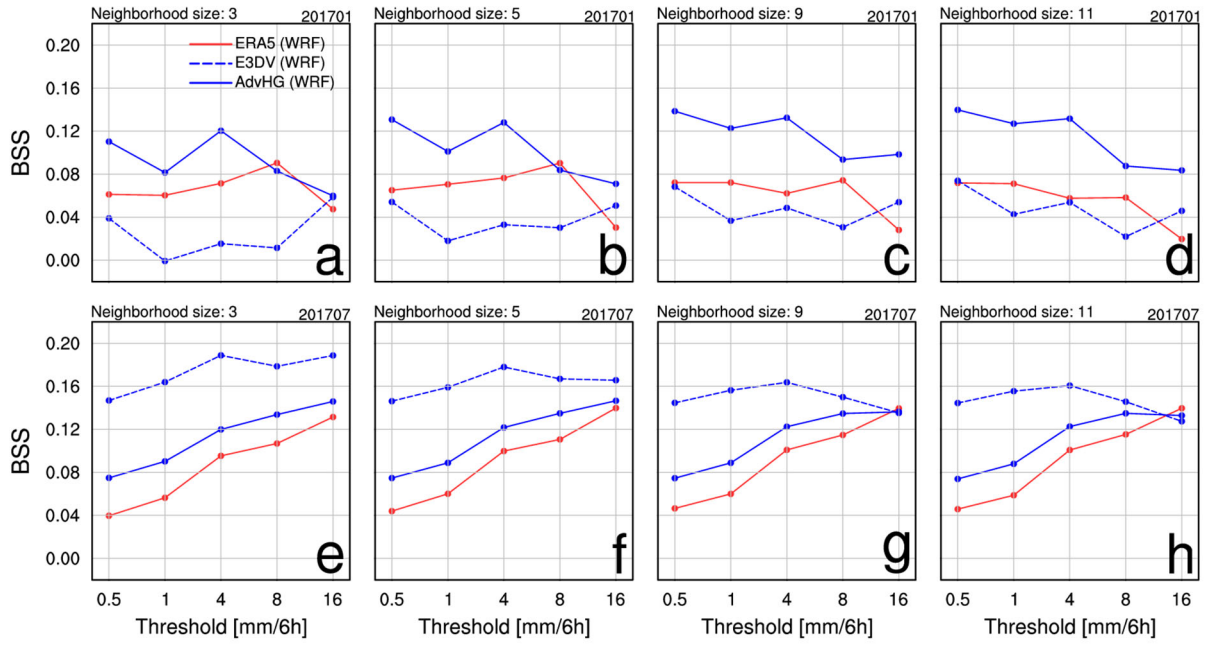
1010



1011

1012 Figure 89. (a,c) POD and (b,d) FAR for (a,b) January and (c,d) July in 2017 depending on
 1013 thresholds 0.5, 1, 4, 8, and 16 mm (6 h)⁻¹.

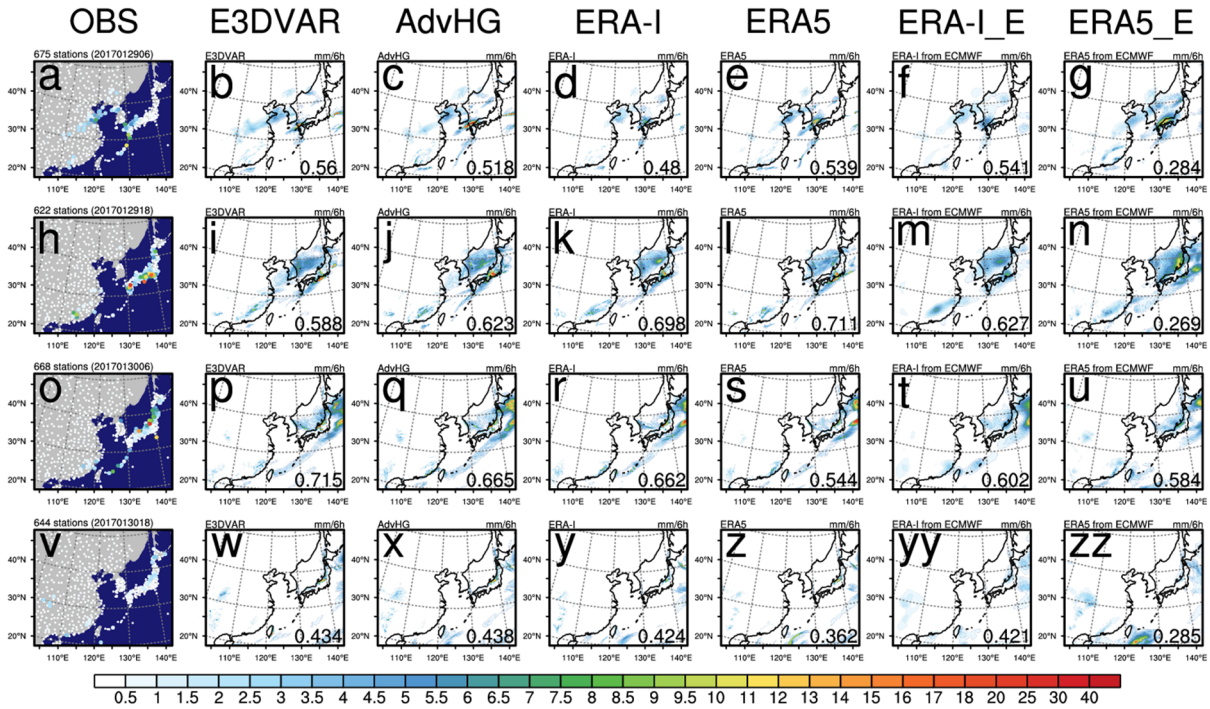
1014



1015

1016 Figure 910. Brier skill score of the probabilistic postprocessed forecast with reference to the
 1017 WRF-based ERA-I for (a-d) January and (e-h) July in 2017 (Blue solid: AdvHG, blue dashed:
 1018 E3DVAR, red solid: WRF-based ERA5).

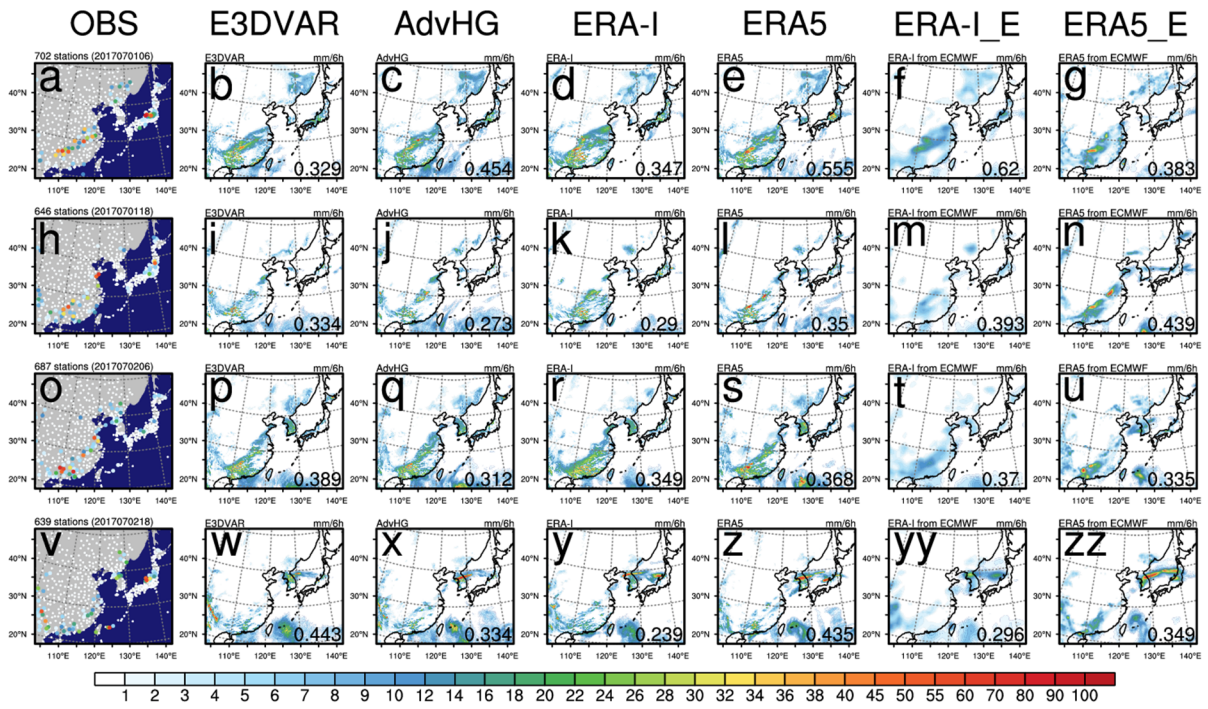
1019



1020

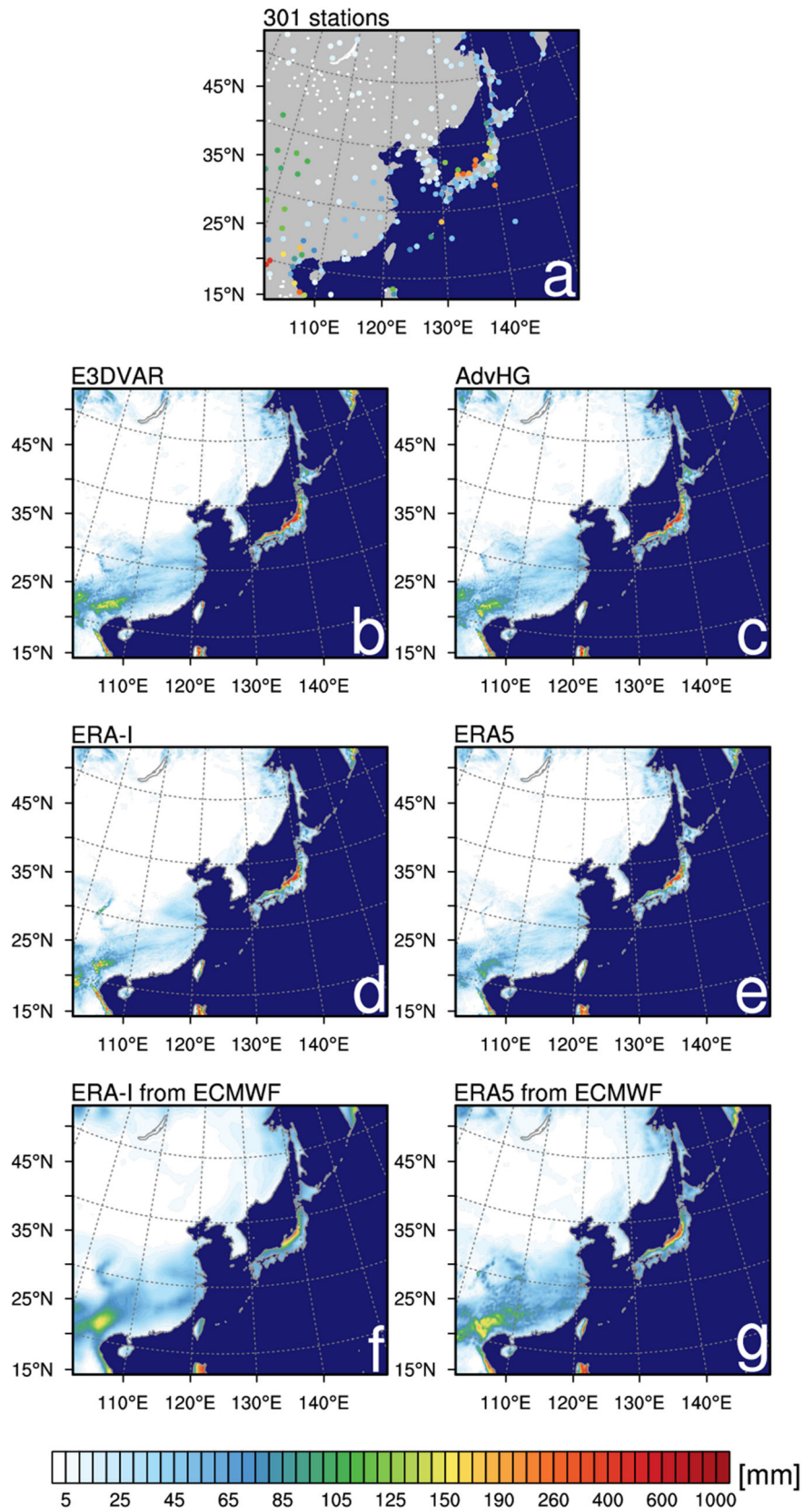
1021 Figure 1011. The spatial distribution of 6 h accumulated precipitation of (1st column)
 1022 observation, (2nd column) E3DVAR, (3rd column) AdvHG, (4th column) ERA-I, (5th column)
 1023 ERA5, (6th column) ERA-I_fromECMWF, and (7th column) ERA5_fromECMWF and the
 1024 pattern correlation coefficient (PCC) shown at the bottom right of each figure at valid time (1st
 1025 low, 3rd low) 06 UTC and (2nd low, 4th low) 18 UTC on 29th and 30th of January in 2017.

1026



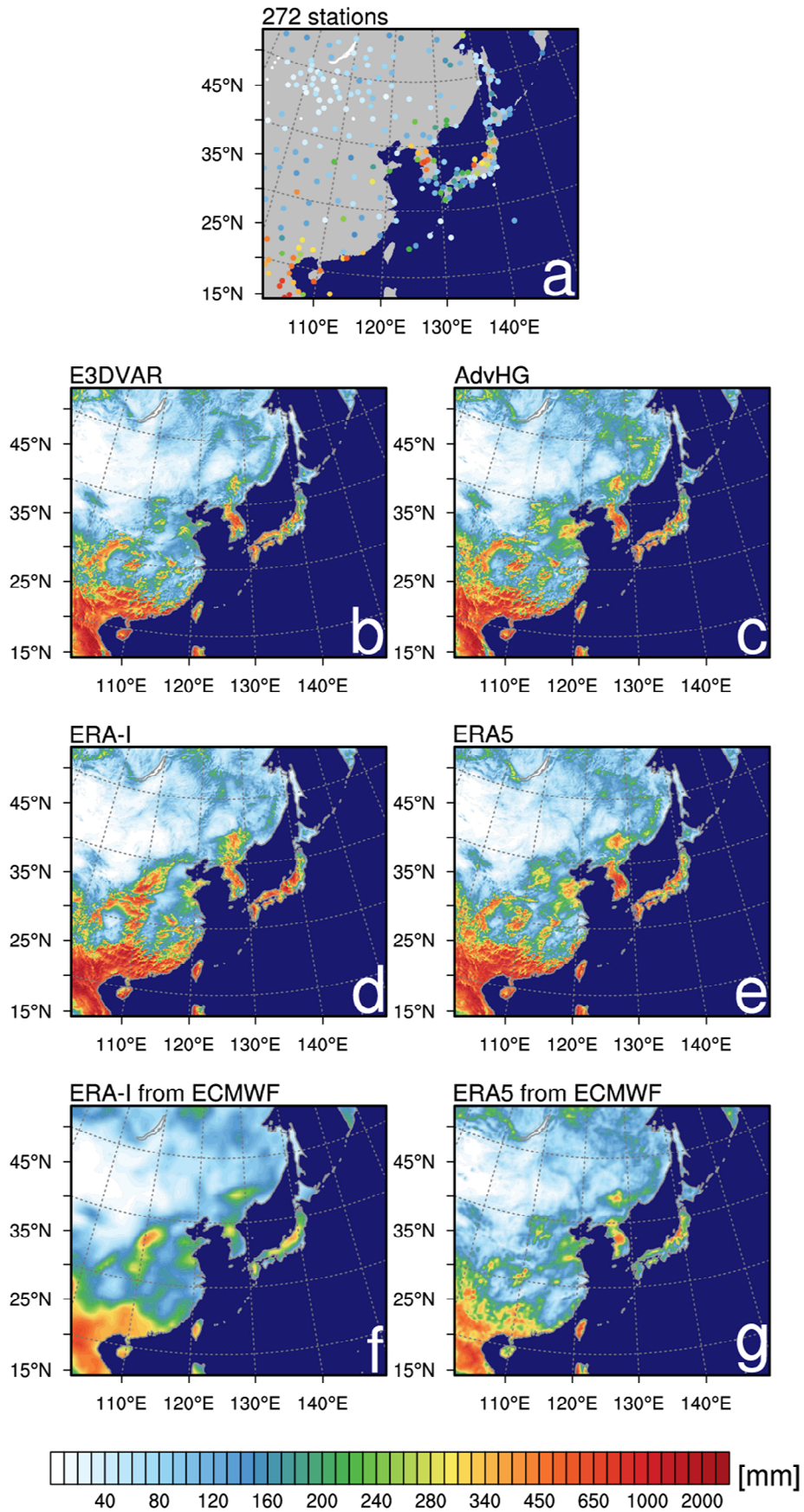
1027

1028 Figure 11. As in Fig. 10, but for 1st and 2nd of July in 2017.



1029

1030 Figure 1213. The spatial distribution of the monthly accumulated precipitation of (a)
 1031 observations, (b) E3DVAR, (c) AdvHG, (d) ERA-I, (e) ERA5, (f) ERA-I from ECMWF, and
 1032 (g) ERA5 from ECMWF for January 2017.



1033

1034 Figure 1314. As in Fig. 1213, but for July 2017.